



Ultra-red Galaxies Signpost Candidate Protoclusters at High Redshift

A. J. R. Lewis¹, R. J. Ivison^{1,2}, P. N. Best¹, J. M. Simpson^{1,3}, A. Weiss⁴, I. Oteo^{1,2}, Z.-Y. Zhang^{1,2}, V. Arumugam^{1,2}, M. N. Bremer⁵, S. C. Chapman³, D. L. Clements⁶, H. Dannerbauer^{7,8}, L. Dunne^{1,9}, S. Eales⁹, S. Maddox^{1,9}, S. J. Oliver¹⁰, A. Omont^{11,12}, D. A. Riechers¹³, S. Serjeant¹⁴, E. Valiante⁹, J. Wardlow¹⁵, P. van der Werf¹⁶, and G. De Zotti¹⁷

¹Institute for Astronomy, University of Edinburgh, Royal Observatory, Blackford Hill, Edinburgh EH9 3HJ, UK

²European Southern Observatory, Karl-Schwarzschild-Straße 2, D-85748 Garching, Germany

³Academia Sinica Institute of Astronomy and Astrophysics, No. 1, Section 4, Roosevelt Road, Taipei 10617, Taiwan

⁴Max-Planck-Institut für Radioastronomie, Auf dem Hügel 69, D-53121 Bonn, Germany

⁵H. H. Wills Physics Laboratory, University of Bristol, Tyndall Avenue, Bristol BS8 1TL, UK

⁶Astrophysics Group, Imperial College London, Blackett Laboratory, Prince Consort Road, London SW7 2AZ, UK

⁷IAC, E-38200 La Laguna, Tenerife, Spain

⁸Departamento de Astrofísica, Universidad de La Laguna, E-38205 La Laguna, Tenerife, Spain

⁹School of Physics & Astronomy, Cardiff University, Queen’s Buildings, The Parade, Cardiff CF24 3AA, UK

¹⁰Astronomy Centre, Department of Physics and Astronomy, University of Sussex, Brighton BN1 9QH, UK

¹¹UPMC Univ Paris 06, UMR 7095, IAP, F-75014, Paris, France

¹²CNRS, UMR7095, IAP, F-75014, Paris, France

¹³Cornell University, Space Sciences Building, Ithaca, NY 14853, USA

¹⁴Department of Physical Sciences, The Open University, Milton Keynes, MK7 6AA, UK

¹⁵Centre for Extragalactic Astronomy, Department of Physics, Durham University, South Road, Durham DH1 3LE, UK

¹⁶Leiden Observatory, Leiden University, P.O. Box 9513, NL-2300 RA Leiden, The Netherlands

¹⁷INAF-Osservatorio Astronomico di Padova, Vicolo dell’Osservatorio 5, I-35122 Padova, Italy

Received 2017 November 13; revised 2018 May 30; accepted 2018 June 12; published 2018 July 26

Abstract

We present images obtained with LABOCA of a sample of 22 galaxies selected via their red *Herschel* SPIRE colors. We aim to see if these luminous, rare, and distant galaxies are signposting dense regions in the early universe. Our 870 μm survey covers an area of $\approx 1 \text{ deg}^2$ down to an average rms of $3.9 \text{ mJy beam}^{-1}$, with our five deepest maps going $\approx 2\times$ deeper still. We catalog 86 dusty star-forming galaxies (DSFGs) around our “signposts,” detected above a significance of 3.5σ . This implies a $100^{+30}_{-30}\%$ overdensity of $S_{870} > 8.5 \text{ mJy}$ (or $L_{\text{FIR}} = 6.7 \times 10^{12} - 2.9 \times 10^{13} L_{\odot}$) DSFGs, excluding our signposts, when comparing our number counts to those in “blank fields.” Thus, we are 99.93% confident that our signposts are pinpointing overdense regions in the universe, and $\approx 95\%$ [50%] confident that these regions are overdense by a factor of at least $\geq 1.5 \times [2\times]$. Using template spectral energy distributions (SEDs) and SPIRE/LABOCA photometry, we derive a median photometric redshift of $z = 3.2 \pm 0.2$ for our signposts, with an inter-quartile range of $z = 2.8 - 3.6$, somewhat higher than expected for $\sim 850 \mu\text{m}$ selected galaxies. We constrain the DSFGs that are likely responsible for this overdensity to within $|\Delta z| \leq 0.65$ of their respective signposts. These “associated” DSFGs are radially distributed within (physical) distances of $1.6 \pm 0.5 \text{ Mpc}$ from their signposts, have median star formation rates (SFRs) of $\approx (1.0 \pm 0.2) \times 10^3 M_{\odot} \text{ yr}^{-1}$ (for a Salpeter stellar initial mass function) and median gas reservoirs of $\sim 1.7 \times 10^{11} M_{\odot}$. These candidate protoclusters have average total SFRs of at least $\approx (2.3 \pm 0.5) \times 10^3 M_{\odot} \text{ yr}^{-1}$ and space densities of $\sim 9 \times 10^{-7} \text{ Mpc}^{-3}$, consistent with the idea that their constituents may evolve to become massive early-type galaxies in the centers of the rich galaxy clusters we see today.

Key words: galaxies: clusters: general – galaxies: high-redshift – galaxies: starburst – infrared: galaxies – submillimeter: galaxies

1. Introduction

Galaxy clusters whose cores are rich in early-type galaxies (ETGs, i.e., relatively passive ellipticals and lenticulars) mark the densest regions in the distribution of dark matter (DM), regions that have grown hierarchically from initial Gaussian fluctuations, supposedly etched into the universe at some arbitrarily early epoch (e.g., Peebles & Yu 1970; White 1978; Spergel et al. 2003). In the local universe, these galaxy clusters harbor the majority of ETGs, which in turn harbor over half of the present-day stellar mass (M_{stars}). Thus studying their cosmic evolution can place valuable constraints on models of galaxy formation (e.g., Springel et al. 2005; Robertson et al. 2007; Overzier et al. 2009a; Lacey et al. 2016).

ETGs obey a tight scaling relation between their color and magnitude, where magnitude approximately equates M_{stars} .

This is known as the “red sequence,” in which more massive galaxies are typically redder with older stellar populations and less ongoing star formation (e.g., Bower et al. 1998, 2006; Baldry et al. 2004; Bell et al. 2004). Furthermore, ETGs in local galaxy clusters appear redder (and thus more massive, since they follow the scaling relation) as their distance to the cluster center decreases (Bernardi et al. 2006). These properties are consistent with the concept of “cosmic downsizing” (Cowie et al. 1996; and see Figure 9 in Thomas et al. 2010), whereby the most massive ETGs formed their stars early ($z \gtrsim 3$) and over relatively short timescales ($\lesssim 0.5 \text{ Gyr}$ —Nelán et al. 2005; Thomas et al. 2005, 2010; Snyder et al. 2012; Tanaka et al. 2013a, 2013b).

ETGs have commonly been viewed as transformed late-type galaxies (LTGs, i.e., star-forming spirals) whose star formation was quenched via some mechanism, leaving behind an ETG on

the red sequence (Dressler et al. 1997; Gerke et al. 2007). In local galaxy clusters this quenching is brought about rapidly via ram pressure stripping (Gunn & Gott 1972) or by so-called “starvation” and/or “strangulation” processes²⁰ (Larson et al. 1980; Balogh et al. 2000; Elbaz et al. 2007; Cooper et al. 2008; Tanaka et al. 2013a; Casado et al. 2015). However, at higher redshifts, could the most massive ETGs, in the centers of galaxy clusters, instead be the remnants of colossal merger events?

An extreme event like this would require wildly different behavior for the precursors of ETGs at $z > 3$, with such systems exhibiting immensely high star formation rates (SFRs, $\psi \sim 10^3 M_{\odot} \text{ yr}^{-1}$). In a hierarchical context, this large burst of star formation is driven by mergers in dense environments (Lacey & Cole 1993). Although the existence of such large systems at such high redshifts places stress on the hierarchical paradigm (Granato et al. 2004), it is conceivable that dusty star-forming galaxies (DSFGs—e.g., Blain et al. 2002; Casey et al. 2014) are associated with these distant events at an epoch when the merger rates are comparatively high (Hine et al. 2016; Delahaye et al. 2017).

Conventional wisdom places this dusty population at $z \sim 2.5$ (Chapman et al. 2005; Simpson et al. 2014), but recent work by Riechers et al. (2013), Dowell et al. (2014), Asboth et al. (2016), and (Ivion et al. 2016, hereafter Paper I), to name but a few, suggests that a rare $z \gtrsim 3$ subset can be identified via their red, far-infrared (far-IR) colors as measured by the Spectral and Photometric Imaging Receiver (SPIRE—Griffin et al. 2010) on board the *Herschel Space Observatory* (Pilbratt et al. 2010). Lensed DSFGs at similarly high redshifts have also been found by surveys at $\lambda_{\text{obs}} > 1 \text{ mm}$ with the South Pole Telescope—relying on flux-density ratios at even longer wavelengths to generate a sample of distant, dust-dominated sources (Vieira et al. 2010; Weiß et al. 2013; Strandet et al. 2016).

With remarkably high median rest-frame, 8–1000 μm luminosities, $L_{\text{far-IR}} = 1.3 \times 10^{13} L_{\odot}$, these so-called “ultra-red galaxies” can provide the SFRs necessary to give birth to the most massive ETGs in the centers of galaxy clusters, and thus, the red sequence. In this work, we go one step further than Paper I exploiting a representative sample of ultra-red galaxies to decipher whether these $z \gtrsim 3$ DSFGs exhibit evidence of clustering consistent with their eventual membership of massive galaxy clusters at $z \sim 0$.

If ultra-red galaxies do indeed trace the precursors of the most massive ETGs in the centers of present-day galaxy clusters, we would expect to witness unvirialized systems characterized by overdensities of (physically associated) DSFGs (i.e., a “protocluster”—Muldrew et al. 2015; Casey 2016). Such systems have already been discovered in the $z > 3$ universe via their submillimeter (submm) emission, with previous work typically relying either on high-redshift radio galaxies (HzRGs—e.g., Ivion et al. 2000; Stevens et al. 2003, 2004; Rigby et al. 2014), pairs of quasi-stellar objects (QSOs—Uchiyama et al. 2017) or even strong overdensities of Ly α emitters as signposts (Tamura et al. 2009; Capak et al. 2011; Tozzi et al. 2015). Predictions by Negrello et al. (2005) suggested that bright-intensity peaks within low-resolution data taken with the *Planck* High Frequency Instrument could

represent clumps of DSFGs. Indeed, overdensities of DSFGs at $z \sim 3$ have been found using this technique (i.e., “HATLAS12-00”—Clements et al. 2016).

Although DSFGs are supposedly poor tracers of large structure below $z \lesssim 2.5$ (Miller et al. 2015), the situation appears to be quite different by $z \sim 5$ (Miller et al. 2016; Oteo et al. 2017b)—although care must be taken when discovering overdensities within such a rare (thus low-numbered) population of galaxy. At odds with this concept is the most-distant ($z \sim 6$) ultra-red galaxy discovered to date, “HFLS 3” (Riechers et al. 2013). Confusion-limited observations of the environments surrounding this DSFG showed little evidence that it signposted an overdensity of DSFGs (Robson et al. 2014). However, in light of new and improved comparison data, it appears that HFLS 3 perhaps signposts a region that is overdense by a factor of at least $\sim 2\times$.

Thus, if our sample of ultra-red galaxies shows an excess of DSFGs compared to the field, we will have confirmed the effectiveness of this novel technique for pinpointing primordial overdensities in the distant universe. Combined with follow-up optical imaging/spectroscopy of their environments (to detect so-called “Lyman-break” galaxies, LBGs—Steidel et al. 1996; Madau et al. 1996), we will be able to place strong constraints on their M_{stars} and DM components. A joint approach—combining models (e.g., Springel et al. 2005) and observations—is necessary to fully predict the eventual fate of these protoclusters at $z \sim 0$ (Casey 2016; Overzier 2016).

The structure of this paper is as follows. In the next section we outline our target sample, as well as our data acquisition and reduction methods. We analyze our data in Section 3 and discuss their implications in Section 4. Finally, our conclusions are presented in Section 5. Throughout our analysis and discussion, we adopt a “concordance cosmology” with $H_0 = 71 \text{ km s}^{-1} \text{ Mpc}^{-1}$, $\Omega_m = 0.27$ and $\Omega_{\Lambda} = 0.73$ (Hinshaw et al. 2009), in which 1' corresponds to a (proper) distance of $\approx 0.5 \text{ Mpc}$ at $z = 3.0$. For a quantity, x , we denote its mean and median values as \bar{x} and $x_{1/2}$, respectively.

2. Target Sample and Data Reduction

2.1. Target Sample

We selected 12 targets—based on their initial shallow $\sim 850 \mu\text{m}$ imaging—from the *H-ATLAS* (*Herschel* Astrophysical Terahertz Large Area Survey—Eales et al. 2010) imaging survey. These targets are contained in Data Release 1 (DR1—Bourne et al. 2016; Valiante et al. 2016) *H-ATLAS* images of the two equatorial Galaxy And Mass Assembly (GAMA 09 and GAMA 15) fields and the South Galactic Pole (SGP) field. Our selection criteria are discussed fully in Paper I, and we briefly outline them here.

We imposed color cuts of $S_{500}/S_{250} \geq 1.5$ and $S_{500}/S_{350} \geq 0.85$ in order to select rare, distant galaxies. We increased the reliability of our ultra-red galaxy sample by imposing a 500 μm significance of $\geq 3.5\sigma_{500}$, and by requiring flux densities consistent with a high redshift in ground-based snapshot images obtained at 850 or 870 μm .

Additionally, we required that $S_{500} \lesssim 100 \text{ mJy}$ in order to reduce the fraction of gravitationally lensed galaxies in favor of intrinsically luminous galaxies (Negrello et al. 2010; Conley et al. 2011), although we draw attention to SGP-28124, with a flux density $S_{500} \approx 120 \text{ mJy}$, which is significantly higher than its cataloged flux density at the time of our observations.

²⁰ Galaxy clusters reside in deep gravitational potentials that heat the intracluster medium (ICM). As a consequence, the ICM strips the cold gas from infalling LTGs and subsequently starves or strangles them of cold gas, which is the fuel for further star formation.

Table 1
Targets and Their Properties

Nickname	α (J2000) δ		t_{int} (hr)	$\bar{\tau}^a$	$\bar{\sigma}^b$ (mJy beam $^{-1}$)	Ω^c (arcmin 2)	Date Observed (yyyy mm)	Program
	($^{\text{h}}$ $^{\text{m}}$ $^{\text{s}}$)	($^{\circ}$ $'$ $''$)						
SGP-28124	00:01:24.73	−35:42:13.7	13.4	0.3	1.9	133	2013 Apr	E-191.A-0748
HeLMS-42	00:03:04.39	+02:40:49.8	0.8	0.3	6.3	121	2013 Oct	M-092.F
SGP-93302	00:06:24.26	−32:30:21.4	16.6	0.3	1.7	129	2013 Apr	E-191.A-0748
ELAIS-S1-18	00:28:51.23	−43:13:51.5	0.9	0.2	5.3	117	2013 Apr	M-091.F
ELAIS-S1-26	00:33:52.52	−45:20:11.9	4.4	0.4	4.0	118	2014 Apr	M-093.F
SGP-208073	00:35:33.82	−28:03:03.2	4.9	0.3	3.2	130	2013 Apr	M-091.F, E-191.A-0748, M-092.F
ELAIS-S1-29	00:37:56.76	−42:15:20.5	2.9	0.3	4.2	137	2013 Oct	M-092.F, M-093.F
SGP-354388	00:42:23.23	−33:43:41.8	11.4	0.3	1.8	124	2013 Oct	M-092.F, E-191.A-0748
SGP-380990	00:46:14.80	−32:18:26.5	4.0	0.3	2.9	115	2012 Nov	M-090.F
HeLMS-10	00:52:58.61	+06:13:19.7	0.5	0.3	8.0	114	2013 Oct	M-092.F
SGP-221606	01:19:18.98	−29:45:14.4	1.3	0.4	6.0	112	2014 May	M-093.F
SGP-146631	01:32:04.35	−31:12:34.6	2.4	0.3	5.0	119	2014 Apr	M-093.F
SGP-278539	01:42:09.08	−32:34:23.0	3.2	0.4	4.4	121	2014 Apr	M-093.F
SGP-142679	01:44:56.46	−28:41:38.3	3.0	0.4	4.3	116	2014 Apr	M-093.F
XMM-LSS-15	02:17:43.86	−03:09:11.2	2.0	0.3	4.4	118	2013 Oct	M-092.F
XMM-LSS-30	02:26:56.52	−03:27:05.0	4.1	0.3	3.4	132	2013 Sep	E-191.A-0748, M-090.F, M-092.F
CDFS-13	03:37:00.91	−29:21:43.6	1.0	0.2	5.3	118	2013 Oct	M-092.F
ADF-S-27	04:36:56.47	−54:38:14.6	3.4	0.3	3.7	135	2012 Sep	M-090.F
ADF-S-32	04:44:10.30	−53:49:31.4	2.0	0.3	5.0	129	2013 Apr	M-091.F, M-092.F
G09-83808	09:00:45.41	+00:41:26.0	9.2	0.3	1.8	125	2013 Oct	E-191.A-0748
G15-82684	14:50:12.91	+01:48:15.0	6.7	0.3	2.3	116	2014 Mar	M-093.F
SGP-433089	22:27:36.98	−33:38:33.9	13.2	0.3	1.8	117	2012 Sep	M-090.F, M-091.F, M-093.F

Notes. Targets are listed in order of increasing R.A.

^a Average opacity value.

^b Average depth computed across each beam-smoothed LABOCA map, where the resulting FWHM of a beam is 27".

^c Extent of LABOCA map.

To this *H*-ATLAS sample, we added an additional 10 targets from five fields in the *HerMES* (*Herschel* Multi-tiered Extragalactic Survey—Oliver et al. 2012) imaging survey—ultra-red galaxies selected in the *Akari Deep Field-South* (ADF-S), the *Chandra Deep Field-South Survey* (CDFS), the European Large-Area Infrared Survey-South 1 (ELAIS-S1), and the *XMM-Large-Scale Survey* (XMM-LSS) fields are contained in the DR4.0 xID250 catalogs by Roseboom et al. (2010, 2012), while those selected from the *HerMES* Large Mode Survey (HeLMS) are among the 477 red galaxies presented by Asboth et al. (2016). All *HerMES* images and catalogs were accessed through the *Herschel* Database in Marseille (HeDaM—Roehlly et al. 2011).²¹

2.2. Observing Strategy

Our sample of 22 ultra-red galaxies were imaged with the Atacama Pathfinder Experiment (APEX) telescope’s Large APEX Bolometer Camera (LABOCA—Kreysa et al. 2003; Siringo et al. 2009) instrument over six observing runs from 2012 September to 2014 March.²² The passband response for this instrument is centered on 870 μm (345 GHz) and has a half-transmission width of $\sim 150 \mu\text{m}$ (~ 60 GHz).

Targets were observed in a compact-raster scanning mode, whereby the telescope scans in an Archimedean spiral for 35 s at four equally spaced raster positions in a 27" \times 27" grid. Each scan was approximately ≈ 7 minutes long such that each raster position was visited three times, leading to a fully

sampled map over the full 11' diameter field of view of LABOCA. An average time of $t_{\text{int}} \approx 4.6$ hr was spent integrating on each target (see Table 1). Maps with longer integration times ($t_{\text{int}} \gtrsim 10$ hr) provide deeper data sensitive to less luminous DSFGs in the vicinity of our signposts. Our shallower maps ($t_{\text{int}} \lesssim 1$ hr) help constrain the abundances of the brightest DSFGs, thus reducing the Poisson noise associated with these rare galaxies. These deep/shallow 870 μm data are necessary to constrain the photometric redshifts of the brighter/fainter DSFGs within the vicinities of our signposts, therefore allowing us to identify members of any candidate protocluster found.

During our observations, we recorded typical precipitable water vapor (PWV) values between 0.4 and 1.3 mm, corresponding to a zenith atmospheric opacity of $\tau = 0.2$ –0.4. Finally, the flux density scale was determined to an rms accuracy of $\sigma_{\text{calib}} \approx 7\%$ using observations of primary calibrators, Uranus and Neptune, while pointing was checked every hour using nearby quasars and found to be stable to $\sigma_{\text{point}} \approx 3''$ (rms).

2.3. From Raw Timestreams to Maps

The data were reduced using the Python-based Bolometer data Analysis Software package (BOA V4.1—Schuller 2012), following the prescription outlined in Section 10.2 and Section 3.1 of Siringo et al. (2009) and Schuller et al. (2009), respectively. We briefly outline the reduction steps below.

1. Timestreams for each scan were calibrated onto the Jy beam $^{-1}$ scale using primary or secondary flux density calibrators.

²¹ <http://hedam.oamp.fr/hermes/>

²² ESO program E-191.A-0748 and MPI programs M-090.F-0025-2012, M-091.F-0021-2013, and M-092.F-0015-2013.

2. Channels exhibiting strong cross talk with their neighbors, showing no signal or high noise were flagged, while the remaining channels were flatfielded.
3. Timestreams were flagged in regions where the speed and acceleration of the telescope are too severe to guarantee reliable positional information at every timestamp.
4. In an iterative manner, the following sequence was performed:
 - (a) Noisy channels were σ -clipped relative to all channels with the degree of clipping increasing from 5 to 3 with each iteration.
 - (b) Sky noise determined across all channels was removed from each channel.
 - (c) Each channel’s timestreams were “despiked” about their mean value.
 - (d) An n th-order polynomial baseline was subtracted from the timestreams to remove any low-frequency drifts, where $n = 1\text{--}4$ with each iteration.
5. Large discontinuities (jumps) in the timestreams, seen in all channels, and correlated noise between groups of channels (e.g., channels sharing the same part of the electronics or being connected to the same cable) were removed.
6. The Fourier spectrum of the timestreams were high-pass filtered below 0.5 Hz using a noise-whitening algorithm to remove the $1/f$ noise. At this stage, the mean noise-weighted point-source sensitivity of all channels was calculated to remove scans corrupted by electronic interference. Uncorrupted scans were opacity-corrected using skydips and radiometer opacity values before being pixelated onto a map. We oversampled the pixelization process by a factor of four to preserve the spatial information in the map. This results in a final map for a given scan with a pixel scale $p \approx 4''.8 \text{ pix}^{-1}$.

We coadded, with inverse weighting, all of the reduced maps for each scan before beam smoothing the final map to ease the detection of point sources and to remove any high-frequency noise on scales smaller than the beam that might exist. The effect of convolving with a Gaussian with a FWHM $\theta = 19''.2$ (i.e., the beam width, see Figure 1) increase the spatial resolution to $\sqrt{\theta^2 + \theta^2} = \sqrt{2}\theta \approx 27''$. Thus we scale the final map by $\sqrt{2}$ in order to preserve the peak intensity, i.e., the mJy beam $^{-1}$ units. As our rms maps are also smoothed by a $19''.2$ Gaussian, we applied an additional scaling to them such that the signal-to-noise ratio (S/N) in regions free of sources was unity.

We repeated these reduction steps, this time using the final reduced map as a model to mask significant sources before flagging the timestreams. Using a model in this fashion helps to increase the final S/N of detections (Nord et al. 2009; Schuller et al. 2009; Belloche et al. 2011). We find that one repetition is sufficient to achieve convergence in the S/N of a point source, in agreement with the findings of Weiß et al. (2009) and Gomez et al. (2010). We present the final S/N maps for all of our ultra-red galaxies in Appendix A.

To model the instrumental noise of our maps, we generated so-called “jackknife” maps by randomly inverting (i.e., multiplying by -1) half of our reduced scans before coadding them. The result is a map free of astronomical sources and confusion, which we estimate to be ≈ 0.9 mJy in our deepest maps, and thus these realizations will underestimate the true noise. For

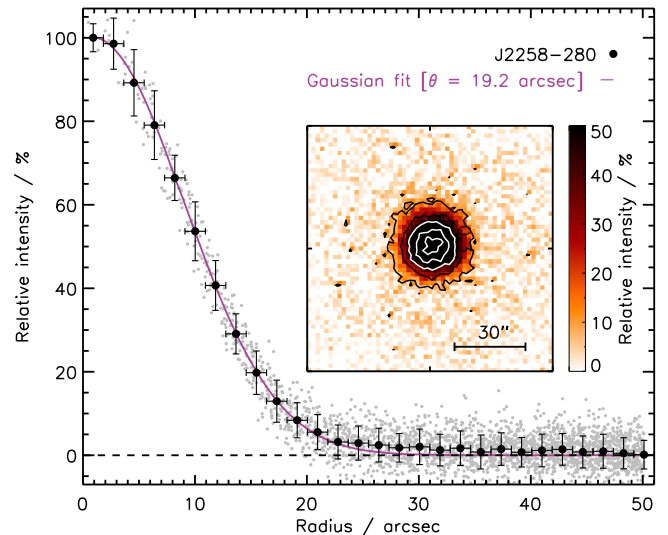


Figure 1. Main: Radially averaged beam profile of J2258–280, the most frequently visited pointing source for this work, reduced in the same manner as our maps. Black points indicate radial bin averages and their respective rms values, after sky subtraction. The beam is well described by a Gaussian with FWHM $\theta = 19''.2$ (purple line), which we use to beam-smooth our final maps. Inset: Normalized flux map of J2258–280 ($S_\nu = 765.4 \pm 26.2$ mJy) with contours indicating the 10, 30 (black), 50, 70, and 99 (white)% peak flux levels.

each map, we created 100 jackknife realizations of the instrumental noise.

In Figure 2 we show the pixel distributions of the final S/N maps and their respective jackknife realizations. There is clearly a positive excess above $S/N \gtrsim 3$ in the final reduced maps compared to the jackknife maps. This excess is caused by the presence of astronomical sources.

3. Analysis

We chose a detection threshold (Σ_{thresh}) based on the values of a “fidelity” or “trustworthiness” parameter, \mathcal{F} , similar to that outlined in Aravena et al. (2016). For all of our maps, we ran our extraction algorithm (Section 3.1) and compared the number of sources detected in our maps, \mathcal{N} , to the mean number of sources detected in our 100 jackknife realizations for each map, $\overline{\mathcal{N}}_{\text{jack}}$, as a function of detection S/N:

$$\mathcal{F} = 1 - \frac{\overline{\mathcal{N}}_{\text{jack}}}{\mathcal{N}}. \quad (1)$$

We show the average fidelity in the right-hand panel of Figure 2, which illustrates that by increasing the detection S/N, we increase our confidence in the recovered sources. We reach a fidelity of $\mathcal{F} \approx 100\%$ at $\gtrsim 5\sigma$ and a fidelity of $\mathcal{F} = 50\%$ at $\approx 3\sigma$, the latter indicating that we would expect about half of our sources to be spurious at $S/N \approx 3$. We chose—as a compromise between reliability and the number of cataloged sources—a detection threshold of $\Sigma_{\text{thresh}} > 3.5$, where we have a fidelity $\mathcal{F} \approx 65 \pm 8\%$.

The intrinsic map-to-map scatter in the fidelity is caused by the varying abundance of sources in each map, due to the effects of cosmic variance and the differing rms noise levels. This scatter decreases with increasing detection threshold and is $\sigma_{\mathcal{F}} \approx \pm 3\%$ at 5σ .

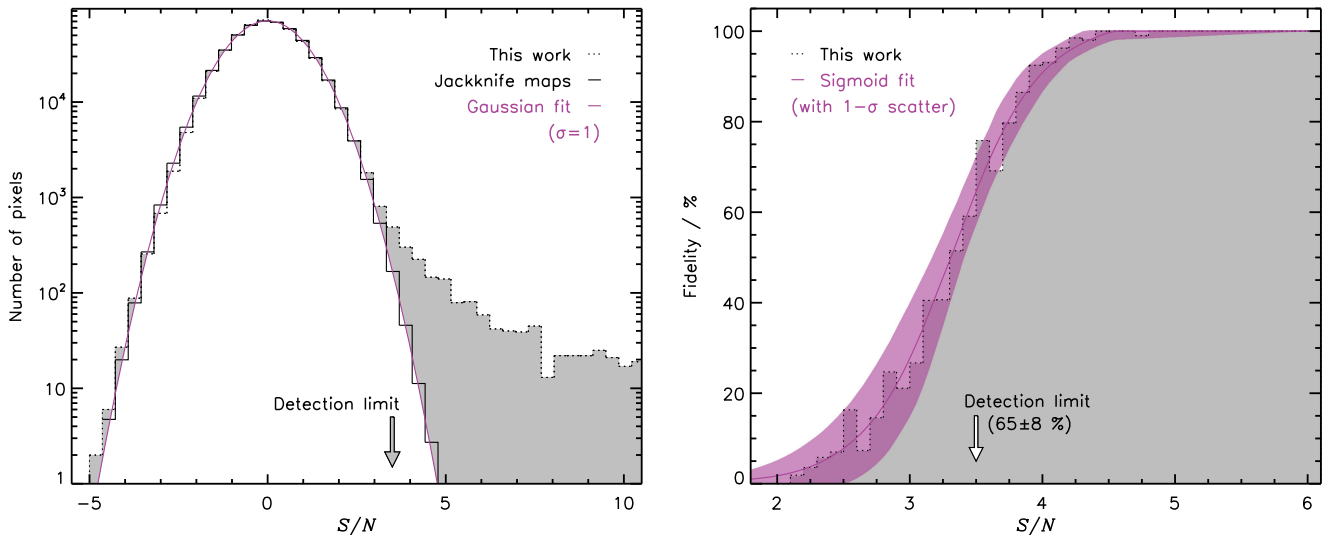


Figure 2. Left: Beam-smoothed S/N pixel distribution for our maps (dotted, black histogram) that shows an excess above our detection threshold due to the presence of astrophysical sources (gray region). We also plot the beam-smoothed S/N pixel distribution of our jackknife maps (black solid histogram, see Section 2.3), whose mean is well modeled by a Gaussian (solid, purple line) centered on $\mu = 0$ with a standard deviation $\sigma = 1$, as expected. Right: Mean fidelity (black, solid histogram — \mathcal{F}) as a function of detection S/N for our maps using our extraction algorithm (see Section 3.1). We parameterize the histogram by a sigmoid function (purple, solid line), which we use to deduce the fidelity of each source detected. We draw attention to the fact that this is a statistical measurement and that on average $65 \pm 8\%$ of sources detected at 3.5σ will be trustworthy, i.e., a third of these sources may be spurious.

3.1. Source Extraction

We used a custom-written Interactive Data Language (IDL—Landsman 1993) source-extraction algorithm to identify and extract sources in the beam-smoothed S/N maps, noting that the beam-smoothing step described above optimizes the detection of point sources.

In a top-down fashion, we searched for pixels above our floor S/N detection threshold $\Sigma_{\text{thresh}} > 3.5\sigma$. To accommodate sources whose true peak falls between pixels, we temporarily lowered Σ_{thresh} by $\approx 95\%$, keeping sources with bicubically interpolated sub-pixel values that meet our original S/N detection threshold. In Table 5 we catalog the peak flux density, noise, and position determined from a three-parameter Gaussian fit made inside a box of width θ (i.e., $\approx 27''$) centered on a source. After removing the fit from the map, we searched for and cataloged subsequent peaks until no more could be found.

During the extraction process we performed some additional steps: the parameters of sources deemed too close to each other ($\Delta r < \theta/2$) were reevaluated by fitting multiple three-parameter Gaussians simultaneously; sources deemed too close ($\Delta r < \theta/2$) to the map edges were rejected.

3.1.1. Completeness, Flux Boosting, and Positional Offsets

We inserted simulated sources into our jackknife maps to quantify the statistical properties of our cataloged sources. To ensure that we did not encode any clustering, we randomize the injection sites of our simulated sources. We drew model flux densities down to $S_{\text{mod}} = 1$ mJy from a Schechter function parameterization of the number counts,

$$\frac{dN}{dS_{\text{mod}}} \propto \left(\frac{S_{\text{mod}}}{S_0} \right)^{-\alpha} e^{-S_{\text{mod}}/S_0}, \quad (2)$$

where $S_0 = 3.7$ mJy and $\alpha = 1.4$ (Casey et al. 2013), which we scaled to $870 \mu\text{m}$ using a spectral index of ν^2 , i.e., we divided the model fluxes by $(\nu_{870}/\nu_{850})^2 \approx 1.05$.

For each simulated source, we ran our source-extraction algorithm, and if we detected a peak within a threshold radius, $r_{\text{thresh}} \leq 1.5 \times \theta$, of the injection site, then we recorded the best-fitting Gaussian parameters. If we recovered multiple peaks within our threshold radius, we took the most significant. Finally, if we failed to recover a simulated source, we recorded the model flux density and the instrumental noise at the injection site.

This procedure was repeated 10,000 times for each target so that we generated a large, realistic catalog of simulated sources. We used this to determine the noise-dependent completeness, \mathcal{C} , i.e., the fraction of recovered sources to input sources, as well as the flux boosting, \mathcal{B} , i.e., the ratio of recovered to input flux densities, and the radial offsets, \mathcal{R} , i.e., the distance between recovered and input positions for each cataloged source.

We calculated the median flux boosting in bins of recovered S/N, which we used to translate the recovered flux densities of our detections into model flux densities (see Figure 3). After this stage, we used our deboosted flux densities with their associated instrumental noise levels to determine their completenesses and radial offsets. The former we computed from a spline interpolation of a two-dimensional surface of modeled flux density and instrumental noise (see Figure 4 and, e.g., Geach et al. 2013), while the latter we computed from a spline interpolation of modeled S/N (see left-hand panel of Figure 5).

At our detection threshold, the flux density of a source in our deepest map, SGP-93302, is typically boosted by $\mathcal{B} = 1.7$, which is in agreement with the literature at similar depths (e.g., $\mathcal{B} \approx 1.5$ —Geach et al. 2017), while at $S/N \gtrsim 6$, the flux boosting becomes negligible. However, we draw attention to the relatively severe deboosting factors recorded for our noisiest maps (e.g., central rms, $\sigma \gtrsim 5$ mJy for SGP-221606) due to the steep bright-end ($S_\nu > 13$ mJy) slope of the number counts.

For SGP-93302, our two-dimensional completeness function indicates that we are $\mathcal{C} \approx 100\%$ complete at a deboosted

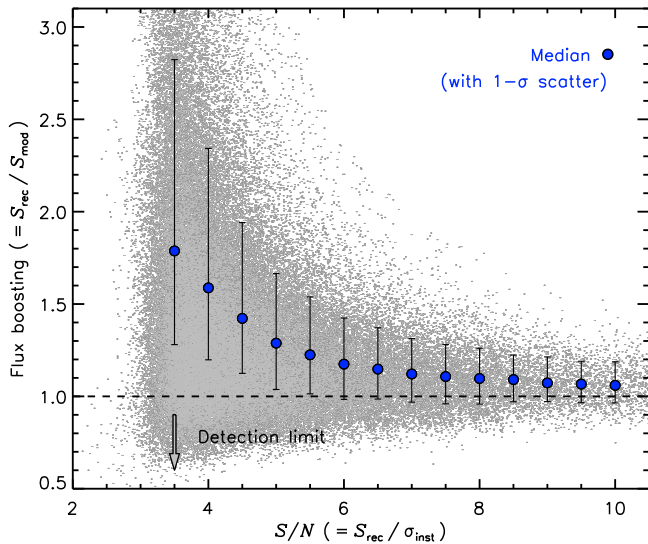


Figure 3. Flux boosting (i.e., recovered vs. modeled flux density) as a function of recovered S/N for SGP-93302. We generate a model flux density distribution using the Schechter parameterization of the number counts given in Casey et al. (2013) when determining these corrections. We record a negligible flux-boosting factor, $\mathcal{B} < 1.1$, at $S/N \gtrsim 6.0$ and witness corrections of $\mathcal{B} \approx 1.7$ at our detection threshold, comparable to that of S2CLS ($\mathcal{B} \approx 1.5$ —Geach et al. 2017), despite the different noise levels.

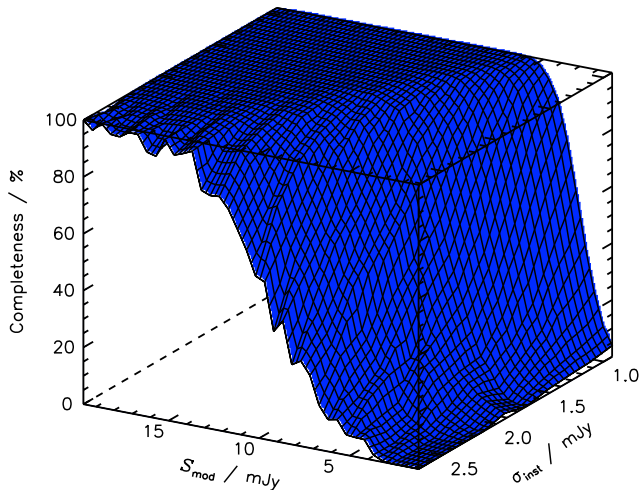


Figure 4. Completeness for SGP-93302 as a function of instrumental noise and model flux density. The two-dimensional treatment of our completeness is vital due to the radially varying sensitivity across our maps. We see that as the instrumental noise decreases and our model flux density increases, our completeness increases as well. For this map, at an instrumental noise and model flux density of $\sigma_{\text{inst}} \approx 1.2$ mJy and $S_{\text{mod}} \approx 1$ mJy, respectively, we recover hardly any sources, i.e., $\mathcal{C} \approx 0\%$. However, increasing the model flux density to $\gtrsim 5$ mJy while keeping the noise constant results in most sources being recovered successfully, i.e., $\mathcal{C} \approx 100\%$.

flux density and instrumental noise of $S_{\text{mod}} \approx 5$ mJy and $\sigma_{\text{inst}} \approx 1.2$ mJy, respectively. In this same flux density plane, our completeness falls close to $\mathcal{C} \approx 0\%$ as the instrumental noise reaches $\sigma_{\text{inst}} \approx 2.5$ mJy.

In the left-hand panel of Figure 5 we see that the mean radial offset is in good agreement with that expected from Equation (B22) in Ivison et al. (2007). There exists a large scatter in the low $S/N \lesssim 5$ bins, which indicates that our radial offsets at a given S/N value can vary by as much as $\sigma_{\mathcal{R}} = \pm 2''.5$. We also note that our brightest detections with $S/N \approx 30$ have radial

offsets as little as $\mathcal{R} = 0''.5$, allowing us to accurately constrain the positions of such sources.

Finally, the simulated sources that we successfully recovered match the Schechter source counts given in Equation (2) to within 1σ , with no underlying systematics remaining.

3.2. Herschel SPIRE Photometry

In order to derive photometric redshifts for the LABOCA-detected DSFGs, we bicubically interpolated the SPIRE flux-density maps at the LABOCA source positions. We determined the errors and local sky values from a box of width $\approx 12 \times \theta_{\text{SPIRE}}$ centered on each detection, where $\theta_{\text{SPIRE}} \approx 18'', 24''$ and $35''$ for the 250, 350 and 500 μm passbands, respectively (Valiante et al. 2016).

To quantify the effect that the LABOCA radial offset has on determining our SPIRE measurements, we analyzed how the “true flux density” of a source varied as we tweaked the position at which we measured it. For each survey field and passband, we selected a bright ($S_{250} \approx S_{350} \approx S_{500} \approx 1$ Jy) point source and measured the true flux density at its cataloged position. We then performed 500 Monte Carlo simulations, drawing radial offset values from a Gaussian distribution centered on the cataloged position with a standard deviation²³ $\sigma = \mathcal{R}$, which we allowed to range across $\mathcal{R} = 0''\text{--}10''$. For each simulation, we measured the flux density at the adjusted positions and compared them to the true flux density. We used this ratio (F_{rec}) to flux-boost a SPIRE photometric measurement, depending on the LABOCA radial offset it exhibited. We parameterize this value using $F_{\text{rec}}/\% = 100 - (\mathcal{R} / \alpha)^\beta$, where $\alpha = 1.0, 1.4,$ and 1.9 and $\beta = 1.7, 1.8,$ and 1.9 at 250, 350, and 500 μm , respectively.

The right-hand panel of Figure 5 shows that the average radial offset is passband related, reflecting the different pixel scalings of $6'', 8''.3$ and $12'' \text{pix}^{-1}$ for the 250, 350, and 500 μm passbands in *H-ATLAS*, respectively (similar values are recorded in *HerMES*). We see that for detections with low radial offsets, $\mathcal{R} < 2''$, and thus high $S/N \gtrsim 8$ values, we recover $\approx 95\%$ of the true flux density. Owing to the large SPIRE 500 μm pixel size, even at the highest radial offsets considered in this paper ($\mathcal{R} \approx 10''$) for sources near to or at our detection threshold, we still recover $\gtrsim 80\%$ of the true flux density. Conversely, however, we only recover $\gtrsim 55\%$ and $\gtrsim 65\%$ of the true flux densities for these highest offsets at 250 and 350 μm , respectively.

We draw attention to 16 (i.e., $\approx 15\%$) of our LABOCA sources that are undetected at the 1σ level in all SPIRE maps. The majority (12) of these possibly spurious sources have detection $S/N \lesssim 4.5$, in agreement with our fidelity analysis. The number of sources with higher S/N values is also expected when the intrinsic scatter in the fidelity parameter is taken into account. These sources do not affect our number counts because on average, we correct for this effect. Thus our fidelity $\mathcal{F} = 65 \pm 8\%$ and high flux-boosting factors at these low S/N thresholds weights these possibly spurious sources accordingly. However, we choose not to include any of these sources in our photometric redshift analysis—we are unable to meaningfully constrain them.

²³ As \mathcal{R} is defined as the radial distance from the injected to the recovered position of a simulated source, we vary each coordinate of each spatial dimension (α and δ) by $\mathcal{R}_\alpha = \mathcal{R}_\delta = \mathcal{R}/\sqrt{2}$.

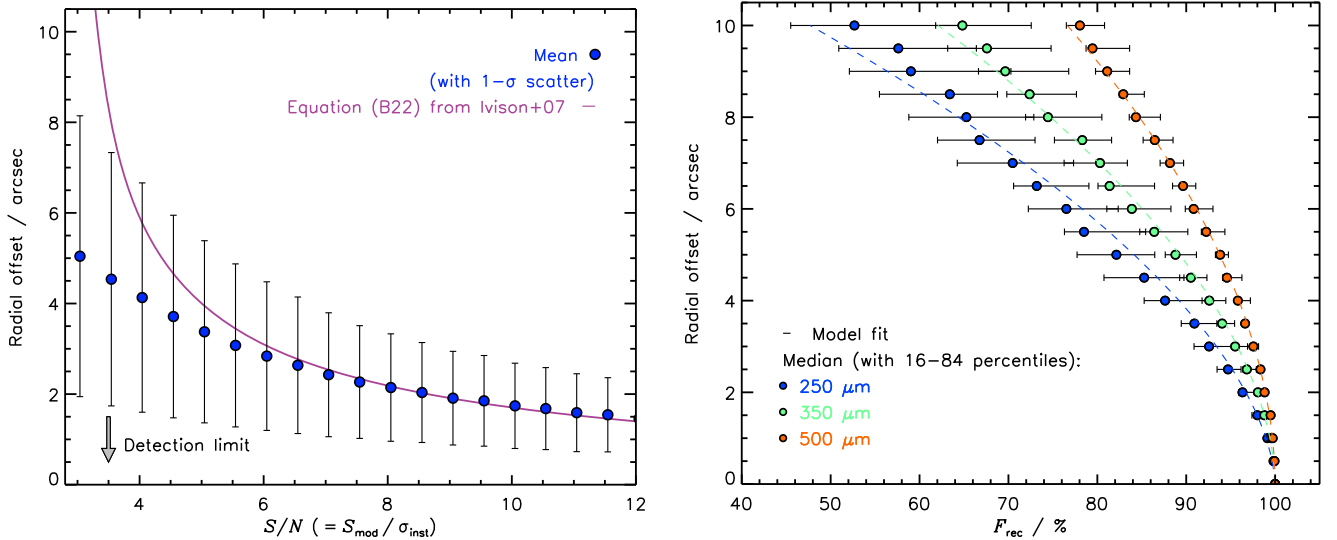


Figure 5. Left: Radial offset (\mathcal{R} , difference between the model and recovered source position) as a function of modeled S/N for SGP-93302. The 1σ errors for each bin are taken from the rms of the radial offsets in that S/N bin. We also plot the predicted form given by Equation (B22) in Ivison et al. (2007) using the number counts of LESS, which is in good agreement. Right: SPIRE flux boosting to accommodate the drop in measured flux density due to the LABOCA radial offset (left-hand panel) as deduced from our Monte Carlo simulations. The colored circles represent the median with errors from the 16th and 84th percentiles from the median across all of the SPIRE survey fields. We see that at $\mathcal{R} = 4''$, roughly equating to a modeled S/N ≈ 5 , we recover 85%, 92%, and 97% of the flux density across the 250, 350, and 500 μm passbands, respectively. This decreasing loss of flux represents the increasing optimal pixel sizes due to the differing SPIRE beam sizes.

Finally, we note that the SPIRE fluxes derived in this manner, i.e., using a LABOCA prior and a radial offset flux-boosting value, are consistent with those from which they were originally selected—varying by $\pm 1\sigma$.

3.3. Photometric Redshifts

We use a custom-written χ^2 -minimization routine in IDL to determine far-IR-based photometric redshifts for our catalog of sources, which have at least one SPIRE detection above $>1\sigma_{\text{SPIRE}}$. We fit to three well-sampled spectral energy distributions (SEDs) used in Paper I: that of the Cosmic Eyelash (Ivison et al. 2010; Swinbank et al. 2010), and synthesized templates from Pope et al. (2008) and Swinbank et al. (2014), ALESS. Figure 4 in Paper I highlights the diversity of these SEDs in the rest frame, each normalized in flux density at $\lambda_{\text{rest}} = 100 \mu\text{m}$.

We use the deboosted 870 μm and boosted SPIRE flux densities during our template fitting. The fitting is done in linear space (accommodating for negative fluxes) over a photometric redshift range $0 < z_{\text{phot}} < 10$ down to a resolution of $\Delta z = 0.01$. We adopt the photometric redshift associated with the template that produces the overall minimum χ^2 value (χ^2_{min}) and report 1σ errors based on the $\chi^2_{\text{min}} + 1$ values. We find that the errors determined in this way are consistent with the Monte Carlo method used in Paper I. However, they are inconsistent with the intrinsic scatter deduced from a training sample of spectroscopically confirmed DSFGs that meet our ultra-red criteria. In Paper I, we find that the accuracy and scatter in $\Delta z / (1 + z_{\text{spec}}) = (z_{\text{phot}} - z_{\text{spec}}) / (1 + z_{\text{spec}})$ are $\mu_{\Delta z} = -0.03(1 + z_{\text{spec}})$ and $\sigma_{\Delta z} = 0.14(1 + z_{\text{spec}})$, respectively. This scatter is representative of the minimum systematic uncertainty when determining photometric redshifts using these three templates—significantly larger than that determined from both the $\chi^2_{\text{min}} + 1$ values at high redshift.

The results of these fits, as well as the rest-frame 8–1000 μm luminosities are presented in Table 4.

4. Discussion

We catalog 108 DSFGs from our 22 maps above $\Sigma_{\text{thresh}} > 3.5$ and list their SPIRE and LABOCA flux densities and their mean flux boosting, $\bar{\mathcal{B}}$, and mean fidelity, $\bar{\mathcal{F}}$, parameters in Table 5. Our signpost ultra-red galaxies span a deboosted flux density range of $S_{870} = 2.9\text{--}42.8$ mJy, with a mean $\bar{S}_{870} = 17.0$ mJy. The surrounding field galaxies span a deboosted flux density range of $S_{870} = 1.9\text{--}31.3$ mJy with a mean $\bar{S}_{870} = 6.8$ mJy. There are two exceptionally bright, new DSFGs with $S_{870} \gtrsim 25$ mJy, but on average, the new field galaxies are less bright than our target ultra-red galaxies.

We are unable to detect four of our target ultra-red galaxies above our S/N > 3.5 threshold; all of these are located in our shallower maps. In such cases, we report the peak flux and rms pixel value within a $45''$ aperture centered on the telescope pointing position. We do not provide completeness, flux-boosting, fidelity, or radial offset values for these sources.

4.1. Number Counts

We deduce number counts, which we list in Table 2 and display in the left-hand panel of Figure 6, using the following equation:

$$N(>S') = \sum_{\forall S_i > S'} \frac{\mathcal{F}}{\mathcal{C}\mathcal{A}}, \quad (3)$$

where the sum is over all deboosted flux densities, S_i , greater than some threshold flux, S' . Fidelity corrections, \mathcal{F} , are made using the detected S/N values, while completeness corrections, \mathcal{C} , are made using the deboosted flux densities and instrumental noises. The area surveyed at a recovered flux density, \mathcal{A} , is obtained by cumulating the area across all of our maps where a given flux density is detected above our threshold. These three corrections account for the varying map rms values in our sample.

Table 2
Number Counts and Overdensities

S'^a (mJy)	$N(>S')$ (deg $^{-2}$)	$\mathcal{N}(>S')^b$	$\delta(>S')$	$\bar{\mathcal{C}}$	$\bar{\mathcal{B}}$	$\bar{\mathcal{F}}$
5.5	273.9 $^{+53.7}_{-45.4}$	36 $^{+7}_{-5}$	+0.4 $^{+0.1}_{-0.1}$	0.68	1.54	0.98
7.0	186.4 $^{+39.9}_{-33.3}$	31 $^{+6}_{-5}$	+0.7 $^{+0.2}_{-0.2}$	0.70	1.49	0.98
8.5	109.5 $^{+27.2}_{-22.2}$	24 $^{+5}_{-4}$	+1.0 $^{+0.3}_{-0.3}$	0.74	1.45	0.99
10.0	59.6 $^{+18.9}_{-14.8}$	16 $^{+5}_{-3}$	+1.3 $^{+0.6}_{-0.5}$	0.81	1.42	1.00
11.5	28.2 $^{+10.7}_{-8.0}$	12 $^{+4}_{-3}$	+1.5 $^{+0.9}_{-0.8}$	0.88	1.25	1.00
13.0	23.1 $^{+9.9}_{-7.2}$	10 $^{+4}_{-3}$	+4.0 $^{+3.6}_{-3.4}$	0.88	1.26	1.00
14.5	18.8 $^{+9.3}_{-6.5}$	8 $^{+3}_{-2}$	+11.4 $^{+16.5}_{-16.0}$	0.87	1.26	1.00
16.0	8.4 $^{+5.7}_{-3.6}$	5 $^{+3}_{-2}$	+39.2 $^{+146.3}_{-144.8}$	0.98	1.13	1.00

Notes.

^a Flux-density threshold levels are taken from Weiß et al. (2009) to simplify the comparisons we made with LESS.

^b Represents the raw number of galaxy detected above a given flux-density threshold.

We exclude the target ultra-red galaxies to partially remove the bias associated with imaging a region where a galaxy is already known to reside. We note, however, that this method does not fully remove all of the bias associated with imaging a region centered on a galaxy. The reason is that galaxies themselves are known to cluster (Greve et al. 2004; Weiß et al. 2009). Thus, these “galaxy-centric” regions will be, by definition, overdense relative to arbitrarily selected regions.

The errors on the number counts are deduced using

$$\sigma_{N(>S')} = N(>S') \frac{\sigma_{G86}}{\mathcal{N}(>S')}, \quad (4)$$

where σ_{G86} are the double-sided 1σ Poisson errors (Gehrels 1986) and $\mathcal{N}(>S')$ are the number of sources above each threshold flux density.

Because of the large flux density uncertainties in some of the cataloged DSFGs, we compare the method outlined above to drawing realizations of the flux densities and computing Equation (3) for each realization, adjusting \mathcal{B} , \mathcal{F} and \mathcal{C} accordingly. We then take the median and errors from the 15th and 84th percentiles from the median. We find no significant variation in the results obtained from either method, which suggests that the large flux density uncertainties do not severely affect our number counts analysis.

Our number counts are always $\gtrsim 1\sigma$ above those from the LABOCA Extended *Chandra* Deep Field South (ECDFS) Submillimetre Survey (LESS—Weiß et al. 2009) and the SCUBA-2 Cosmology Legacy Survey (S2CLS—Geach et al. 2017). We see a slight break in the shape of counts at $S' > 7$ mJy, similar to that seen in the LESS number counts.

Figure 6 shows that there are similarities in the shape of our number counts to those of J2142–4423, a Ly α protocluster (Beelen et al. 2008), at $S' \leq 7$ mJy and $S' \geq 14$ mJy. However, it is unclear whether Beelen et al. (2008) removed the target source from their number counts, which, as mentioned earlier, will bias their results higher. Furthermore, Beelen et al. (2008) claim that the environments around J2142–4423 are only moderately overdense compared to SHADES—but as discussed previously, we believe this to be evidence that J2142–4423 is overdense compared to LESS and S2CLS. Figure 6 also shows the number counts of MRC 1138262 (the so-called “Spiderweb

galaxy”—Miley et al. 2006; Dannerbauer et al. 2014), a HzRG with an overdensity of sources compared to LESS at $S' > 7$ mJy (i.e., ≈ 385 deg $^{-2}$). This protocluster is $\approx 2\times$ more overdense compared to our work, but it should be noted that Dannerbauer et al. (2014) neither account for flux boosting nor survey completeness, nor do the authors remove the target galaxy (DKB07). We crudely correct for the first two of these differences using the results obtained for SGP-93302, which was observed under similar conditions for a similar integration time to MRC 1138262. Adjusting for these corrections, we record less extreme number counts of $N(>6$ mJy) $\approx 394 \pm 176$ deg $^{-2}$ (1σ Poisson errors) that exhibit a sharp break at $S' \approx 6.5$ mJy. Thus, MRC 1138–262 has number counts that are only slightly higher than those presented in this work.

In Figure 7 we show how the contribution to our number counts at the flux densities provided in Table 2 varies in two signpost-centric annuli of equal area (16π arcmin 2). We see that at $S' > 8.5$ mJy, $\approx 80\%$ of the contribution to the number counts comes from DSFGs distributed within $r_{\text{target}} < 4'$ of our signposts. However, because of the low numbers of galaxies above these deboosted flux-density thresholds, this excess contribution is not significant ($\approx 1.5\sigma$). However, the increasing instrumental noise with distance from our signposts causes comparisons of the number counts at all but the highest flux densities to become heavily biased. We see that at the higher flux-density thresholds, this perceived excess diminishes rapidly, and above $S' > 11.5$ mJy, the contribution appears to be equally split between the two annuli. Thus, without uniformly wide imaging of these environments, the number counts as a function of radial distance remain largely unconstrained for this sample.

Finally, in Figure 8 we show the differential number counts for this work alongside those of the LESS and S2CLS blank fields and the two known protoclusters J2142–4423 and MRC 1138262.

4.2. Overdensities

In order to make a statistical analysis of the significance of our number counts, we employ an overdensity parameter (Morselli et al. 2014)

$$\delta(>S') = \frac{N(>S')}{N(>S')_{\text{blankfield}}} - 1, \quad (5)$$

where $N(>S')_{\text{blankfield}}$ are the number counts expected in a blank-field survey above some threshold flux density.

When choosing a blank-field survey suitable for comparison, it is important to compare “like-for-like” (i.e., Condon 2007). For instance, broad-beam surveys can hide the multiplicity of DSFGs; multiplicity was first identified in early interferometric observations with the Very Large Array (VLA)/SMA/Plateau de Bure Interferometer (PdBI; e.g., Tacconi et al. 2006; Ivison et al. 2007; Biggs et al. 2011; Wang et al. 2011; Barger et al. 2012; Smolčić et al. 2012), confirmed for large samples using ALMA observations (Karim et al. 2013; Bussmann et al. 2015; Simpson et al. 2015; Oteo et al. 2017a), and is consistent with models of galaxy formation (e.g., Smolčić et al. 2012; Narayanan et al. 2015). Furthermore, similar—if not identical—data reduction techniques ensure consistency in the flux densities and associated errors, which may otherwise lead to a lower or higher estimate of the number counts (see Section 4.2.1).

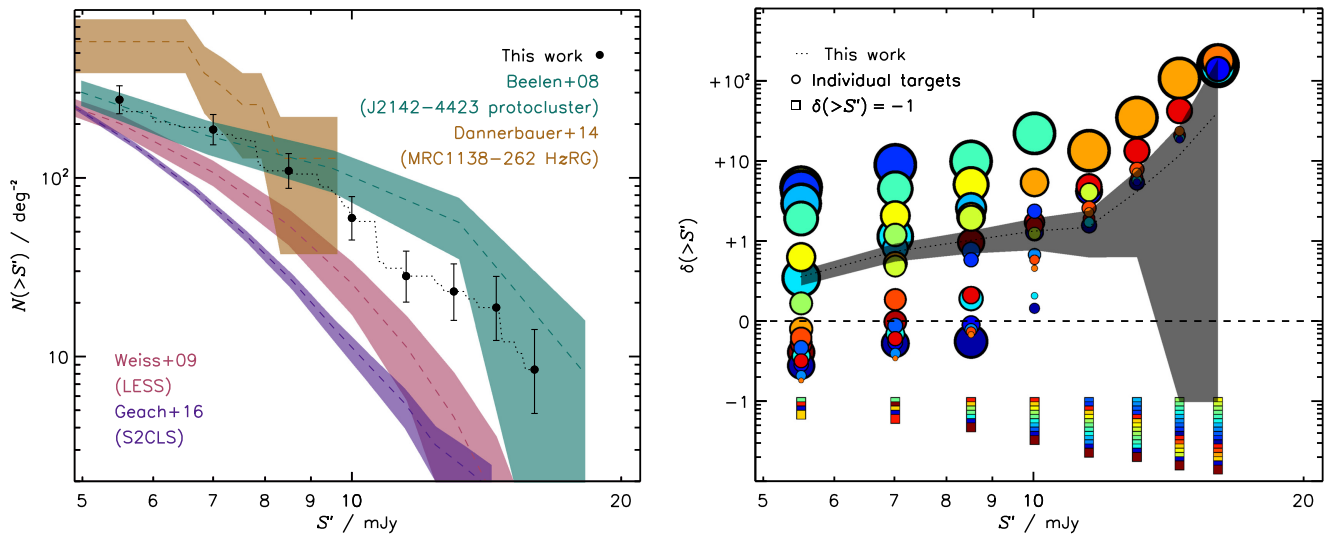


Figure 6. Left: Number counts (excluding our target ultra-red galaxies) as a function of $870 \mu\text{m}$ flux density (black circles) with 1σ double-sided Poisson errors (Gehrels 1986). We show the blank-field number counts from LESS (pink region) and S2CLS (purple region—scaled with a spectral index of ν^2) surveys. We also show the number counts of two known protoclusters, J2142–4423 (green region—Beelen et al. 2008) and MRC 1138262 (brown region—Dannerbauer et al. 2014). It is clearly evident that our number counts are high at all flux density thresholds and exhibit a slight break at $S' > 7 \text{ mJy}$. We believe that the increasing excess at higher flux densities is the result of our ultra-red galaxies signposting similarly extreme DSFGs. Our catalog contains five bright ($S_{870} > 16 \text{ mJy}$) sources. However, we concede that we are unable to rule out gravitational lensing by chance alignment as a cause for the bright sources without high-resolution imaging. Right: Number counts relative to LESS, i.e., the overdensity parameter, $\delta(>S')$. In black we show the results for the entire sample (i.e., the circles from the left-hand panel), while in colored circles we show the overdensity for each map. The size of each circle has been logarithmically scaled to show the influence that each target has in deducing the number counts for the whole sample. Maps where no sources are present above a given threshold flux are indicated by staggered squares starting from $\delta < -1$ for clarity. These squares highlight the deficit of sources due to intrinsic properties (i.e., cosmic variance) and varying map rms values. Hence, we see that some maps probe considerably more overdense regions than others, with variations being sometimes as high ≈ 5 . Finally, we color-code each target from blue to red in order of increasing R.A., i.e., in the order that our targets appear in Table 1 and the color that they have in Figure 13.

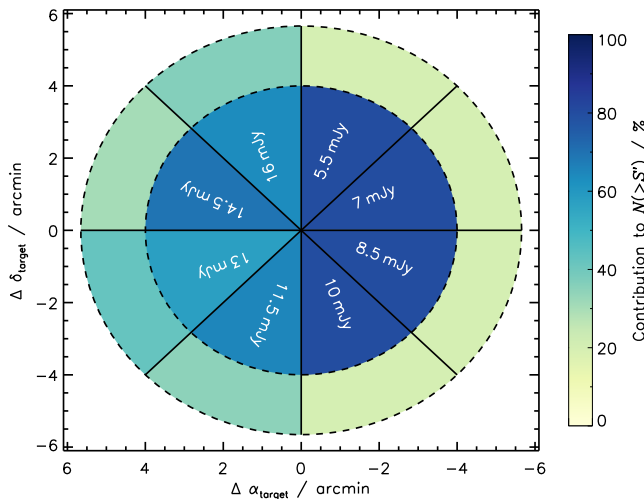


Figure 7. Contribution to the cumulative number counts from two signpost-centric annuli with equal area (i.e., $16\pi \text{ arcmin}^2$). We separate each annuli by dashed black lines and divide them into eight equally sized segments representing the $870 \mu\text{m}$ flux-density thresholds listed in Table 2. We color-code the contribution to the total number counts from each annuli in a given segment (see scale). At $S' < 8.5 \text{ mJy}$, we see that the inner annuli contributes $\approx 80\%$ of the sources responsible for the total number counts. However, by $S' > 11.5 \text{ mJy}$, the contribution is equally split between the two annuli, within the large Poisson errors ($\sigma \approx 30\%$). This highlights the difficulty in claiming any radial dependence on the number counts due to variations in the instrumental noise (i.e., the noise increases as the distance from our signposts increases).

Hence, we choose the LESS number counts (calculated directly from the source catalog) to make comparisons. These data and ours were obtained from the same instrument and are reduced in a similar manner using the same software. However,

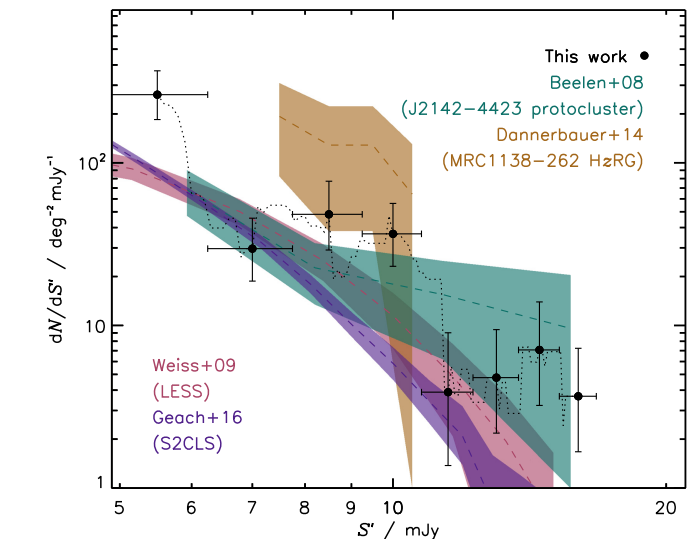


Figure 8. Differential number counts (excluding our target ultra-red galaxies) as a function of $870 \mu\text{m}$ flux density (black circles). As in Figure 6, we also show the differential number counts for the LESS (pink) and S2CLS (purple) blank fields as well as the two known protoclusters J2142–4423 (green) and MRC 1138262 (brown). We see that above $S' > 8.5 \text{ mJy}$, our differential number counts are typically 1σ greater than those presented in LESS—our comparison field of choice.

there are slight differences in the results when we run our source-extraction algorithm on the LESS DR1.0 S/N map.²⁴ Using a detection threshold of $\Sigma_{\text{thresh}} > 3.7$, we recover 95% of their sources. Our $870 \mu\text{m}$ flux density measurements are

²⁴ <http://archive.eso.org/cms/eso-data/data-packages/less-data-release-v1-0.html>

comparable to those in Weiß et al. (2009) as we record a mean absolute offset of $|\overline{\Delta S_i}| = 0.4$ mJy. These differences should have a relatively minor effect on comparisons made with the number counts. However, the computation of completeness and flux-boosting parameters do differ. We record $\lesssim 15\%$ differences in the latter at a detection $S/N \approx 3.7$ for sources around SGP-433089, which has a similar (although slightly higher) average depth to LESS. We note that Weiß et al. (2009) claim that LESS is underdense and also shows a deficit of bright sources relative to other blank fields. However, Figure 6 shows that this is clearly not case when adopting the much deeper and wider data from S2CLS as a reference.

We make overdensity comparisons at a flux-density threshold of $S' > 8.5$ mJy, which equates to a surveyed area of $\mathcal{A} \approx 0.2$ deg² at our detection threshold. We choose this flux-density threshold to be directly comparable to LESS. Furthermore, this threshold is high enough to minimize the correction effects needed for our low S/N detections. At the same time, it is low enough such that our results should not drastically change if our bright sources are magnified by $\mu \lesssim 2$.

We add our number-count error bars in quadrature to those given in Weiß et al. (2009). We determine an overdensity of $\delta = 1.0_{-0.3}^{+0.3}$ at $S' > 8.5$ mJy. In other words, we are 99.93% confident that our signposts pinpoint overdense regions in the universe, and we are $\approx 95(50)\%$ confident that these regions are overdense by a factor of at least $\geq 1.5(2)\times$ compared to LESS.

However, we stress that by *only* removing the target galaxy from our number counts analysis, we are left with a “residual bias” due to imaging a region where a galaxy is known to reside. We estimate that this residual bias increases our overdensity parameter by $\delta_{\text{resid. bias}} = 0.23 \pm 0.02$ over the typical map areas ($\pi(6.2_{-0.1}^{+0.3})^2$) that we have surveyed in this work.

Furthermore, we crudely test what effect removing sources with $S/N \leq 4$ and $S/N \leq 4.5$ has on this overdensity calculation. This S/N regime is close enough to our detection threshold such that the completeness corrections and surveyed area values that we apply should be similar. Thus, we derive overdensity values of $\delta = 1.0 \pm 0.3$ and $\delta = 0.7 \pm 0.2$ for sources with $S/N > 4$ and $S/N > 4.5$, respectively. This suggests that despite a non-negligible fraction of sources near our detection threshold potentially being spurious, our overdensity above 8.5 mJy is comprised of secure LABOCA detections.

Finally, we test the effects that cosmic variance has on our ultra-red galaxies and our comparison field of choice, LESS. To do this, we simulate 100 2 deg \times 2 deg images, which we populate with clustered sources—governed by the observed two-point angular correlation function given in Weiß et al. (2009).

For each ultra-red galaxies, we extract a randomly placed sub-image from 22 randomly chosen simulated images, each with an area that matches our LABOCA data given in Table 1. We then calculate the number of sources present in these sub-images and repeat this process 1000 times. The standard deviation of the total number of sources in each of these 1000 repetitions incorporates, in quadrature, the Poisson noise and the noise from cosmic variance, which we estimate to $\approx 15\%$ on the ultra-red galaxy number counts.

For LESS, we extract a randomly placed, LESS-sized sub-image from each of these larger simulated images and compute

the standard deviation—deriving a relative error of $\approx 20\%$ on the LESS number counts.

As both of the effects from cosmic variance are weaker than that accounted for in the Poisson noise ($\approx 40\%$ and $\approx 50\%$, respectively), we do not propagate either into the error budget for our overdensity parameter.

There exists a strong correlation in flux density with our overdensity parameter, as seen in the right-hand panel of Figure 6. Here we plot the overdensity parameter for each target, which we have logarithmically scaled to reflect each target’s contribution to our overall number counts. We see a large scatter across our 22 maps, which is indicative of cosmic variance and varying levels of map noise. The evolution in overdensity increases $\sim 50\times$ from $S' = 7\text{--}16$ mJy, although the Poisson error from the blank-field counts rises steeply at the higher flux densities, exacerbated by the large relative error in the number counts of bright sources in LESS. We believe that this evolution is caused by our ultra-red galaxies signposting regions that contain brighter DSFGs. However, without high-resolution imaging of the environments around our ultra-red galaxies, we cannot rule out gravitational lensing by chance alignment.

4.2.1. Mundane, Not Cosmic, Underdensity in LESS

It is often claimed that LESS exhibits an underdensity of DSFGs—resulting in the introduction and use of (Dannerbauer et al. 2014; Swinbank et al. 2014) a multiplicative “fudge-factor” ($\sim 2\times$) to the number counts presented in Weiß et al. (2009). An “adjustment” of this magnitude would require us to significantly lower the value of the overdensity parameter, if necessary.

This perceived underdensity is concluded against the number counts presented in SHADES (SCUBA Half Degree Extragalactic Survey—Coppin et al. 2006) as it was the largest “like-for-like” survey at the time. Recently, the Subaru/XMM-Newton Deep Field (SXDF)—one of the two extragalactic fields in SHADES—has been reimaged during the S2CLS, which has improved the sensitivity of this field by $\gtrsim 2\times$.

Using these new data, however, we are only able to match 27/60 (45%) of the SXDF detections²⁵ to a counterpart in the S2CLS.²⁶ These “matched” sources have typical offsets of $4''.7 \pm 3''.0$ and deboosted flux densities that are on average $(1.6 \pm 0.1)\times$ greater than those reported in the S2CLS. The 33/60 (55%) “unmatched” detections have a broad range of deboosted flux densities, $S = 3.1\text{--}22.0$ mJy. These values from SHADES are typically $\approx 4\times$ higher than the measurements we make at their respective positions in the S2CLS image.

Thus, if these results were to be replicated for the Lockman Hole East—the second extragalactic field in SHADES—it would appear that the spurious fraction of sources and/or flux-boosting corrections have been miscalculated. Taken together, these findings suggest that the claimed underdensity in LESS and apparent deficit of bright DSFGs is unlikely to be true and unlikely to be biasing the overdensity parameter of our ultra-red galaxies. Furthermore, these findings are very reminiscent of those discussed by Condon (2007), who resolved the inconsistencies amid differing reports of the radio number counts at the time. Thus, in homage, the variance in the number counts between SHADES and LESS appears to be “mundane”

²⁵ <http://www.roe.ac.uk/ifa/shades/dataproducts.html>

²⁶ <http://zenodo.org/record/57792#.W0tnkRiZNE5>

Table 3
Targets and Their Probability of Being Ultra-red

Nickname	P_{UR} (%)
SGP-28124	94.6 ± 0.4
HeLMS-42	87.4 ± 0.4
SGP-93302	67.5 ± 0.2
ELAIS-S1-18	33.4 ± 0.1
ELAIS-S1-26	61.4 ± 0.2
SGP-208073	62.2 ± 0.2
ELAIS-S1-29	65.8 ± 0.2
SGP-354388	93.2 ± 0.4
SGP-380990	71.1 ± 0.3
HeLMS-10	83.6 ± 0.3
SGP-221606	41.8 ± 0.1
SGP-146631	29.9 ± 0.1
SGP-278539	81.0 ± 0.3
SGP-142679	87.5 ± 0.4
XMM-LSS-15	29.5 ± 0.1
XMM-LSS-30	97.1 ± 0.4
CDFS-13	28.5 ± 0.1
ADF-S-27	43.1 ± 0.1
ADF-S-32	16.5 ± 0.0
G09-83808	89.0 ± 0.4
G15-82684	62.6 ± 0.2
SGP-433089	21.7 ± 0.0

Note. Targets are listed in order of increasing R.A., i.e., in the same order as they appear in Table 1.

(likely due to instrumental and analysis effects) rather than “cosmic.”

4.2.2. Probability of Being Ultra-red

As can be seen Table 5, half of our signposts have SPIRE photometry, which is just consistent with them being ultra-red. This motivates us to derive for the first time a probability that a galaxy is actually ultra-red (P_{UR}) based on its SPIRE photometry.²⁷ To this end, we draw 10,000 realizations of the SPIRE photometry from a Gaussian distribution and determine the number of times that these realizations meet our ultra-red criteria outlined in Paper I. By incorporating the photometric errors from all SPIRE bands, we are able to generate a subset of galaxies that are likely to be ultra-red. Finally, we derive 1σ errors assuming Poisson statistics for these ultra-red galaxy probabilities, which we list in Table 3.

In Figure 9 we show how the overdensity parameter above $S' > 8.5$ mJy varies as a function of its probability of being ultra-red for our signposts. Clearly, galaxies that have a higher probability of being ultra-red typically have a much higher overdensity parameter. Furthermore, overdense signposts (i.e., signposts with $\delta > 0$) all have a probability of being ultra-red greater than $P_{UR} \gtrsim 30\%$. This lower limit value is caused by galaxies lying at the boundaries of both of our SPIRE color cuts outlined in Paper I. Above a probability of being ultra-red of $P_{UR} \gtrsim 60\%$, we see that only three ($\approx 20\%$) of our signposts have environments that are consistent with being underdense (i.e., $\delta < 0$). Such a low fraction of underdense environments suggests that using this novel ultra-red-probability technique in

²⁷ These probabilities are calculated by assuming symmetric color uncertainties, and do not take the bias into account that more bluer galaxies will have had their colors scattered redward, into the ultra-red category, than vice versa. However, these are only used as a guide to the likelihood of being ultra-red.

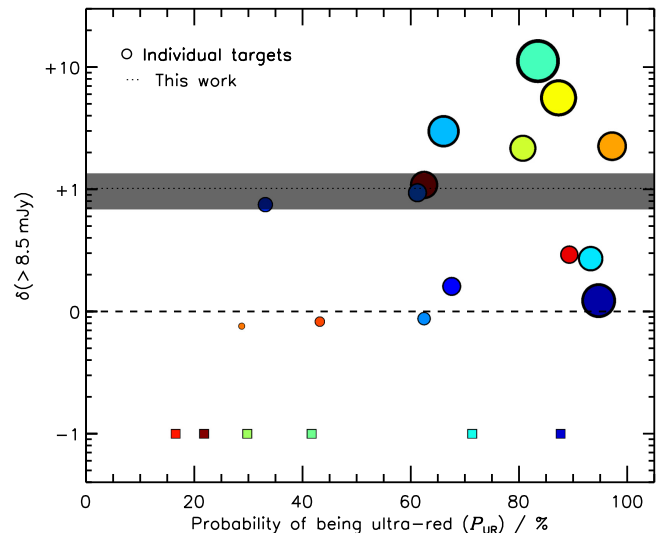


Figure 9. Overdensity parameter above $S' > 8.5$ mJy vs. the probability that our signposts are ultra-red using the method outlined in the text. Each target is color-coded and represented as a circle with a size reflecting its overall contribution to the number counts, i.e., as described in the caption of Figure 6. The mean overdensity at this flux-density threshold is shown as a black dotted line, while the shaded area represents its 1σ uncertainty. This shows that approximately half of our ultra-red galaxies have $P_{UR} \lesssim 68\%$ once their SPIRE flux densities have been reevaluated at their LABOCA position. Conversely, signposts that have a higher probability of being ultra-red contribute more to the mean overdensity at this flux-density threshold.

conjunction with $870 \mu\text{m}$ imaging provides a robust method for signposting overdensities in the distant universe.

4.3. Colors

We analyze the S_{500}/S_{250} and S_{500}/S_{350} colors to see if our field galaxies comprise similarly red galaxies as our signposts. We recall that in the further analysis we exclude 16 LABOCA detections as we are unable to constrain their photometric redshifts. This leaves us with $86 - 16 = 70$ DSFGs around our 22 ultra-red signposts above $> 3.5\sigma$. Figure 10 illustrates that only 7% (≈ 5 DSFGs) of our field galaxies meet our ultra-red galaxy criteria. Such a low fraction might be expected as our ultra-red galaxy criteria select the most luminous and rare DSFGs. If we relax the $3.5\sigma_{500}$ threshold (imposed in Paper I) to $1\sigma_{500}$, our fraction of field ultra-red galaxies increases to 17% (≈ 12 DSFGs) at the expense of being less reliable.

Our field galaxies have median S_{500}/S_{250} and S_{500}/S_{350} colors of $(S_{500}/S_{250})_{1/2} = 1.1$ and $(S_{500}/S_{350})_{1/2} = 0.9$, respectively, with interquartile ranges of $S_{500}/S_{250} = 0.7 - 1.4$ and $S_{500}/S_{350} = 0.7 - 1.2$. If we isolate the field galaxies that we assume to be physically associated with their target galaxy (see Section 4.4), we note a redder change as the S_{500}/S_{250} color increases to a median $(S_{500}/S_{250})_{1/2} = 1.4$ with interquartile range $S_{500}/S_{250} = 1.2 - 1.5$. However, we see no appreciable change in the S_{500}/S_{350} color. As can be seen in Figure 10, this can be explained by five signpost galaxies narrowly missing our original ultra-red criteria when their SPIRE photometry has been remeasured at their LABOCA position.

Thus, if we go one step further and isolate the associated field galaxies that contribute to the overdensity at $S' > 8.5$ mJy, we find that they have redder median colors of $(S_{500}/S_{250})_{1/2} = 1.0$ and $(S_{500}/S_{350})_{1/2} = 1.4$. This is in part due to the exclusion of SGP-433089 and its associated galaxies, which—having had its SPIRE photometry remeasured at the position of its LABOCA

Table 4
Targets and Their Photometric Redshift Properties

ID	z_{phot}^a	χ^2	$\log_{10}(L_{\text{far-IR}})$ (L_{\odot})	ID	z_{phot}^a	χ^2	$\log_{10}(L_{\text{far-IR}})$ (L_{\odot})
SGP-28124							
LURGS J000124.9–354212	$3.4^{+0.1}_{-0.1}$	5.99	$13.50^{+0.02}_{-0.02}$	LURGS J000145.0–353822	$2.5^{+0.2}_{-0.2}$	0.19	$13.05^{+0.05}_{-0.06}$
LURGS J00014.2–354123	$3.6^{+2.0}_{-0.8}$	0.36	$12.59^{+0.30}_{-0.19}$	LURGS J000122.9–354211	$2.5^{+0.2}_{-0.2}$	32.37	$12.95^{+0.05}_{-0.05}$
LURGS J000138.5–35442	$3.7^{+6.3}_{-1.4}$	1.02	$12.38^{+0.64}_{-0.35}$	LURGS J000115.9–35411	$1.6^{+0.4}_{-0.4}$	0.69	$12.36^{+0.17}_{-0.26}$
LURGS J000129.4–354416	$1.6^{+0.4}_{-0.5}$	2.20	$12.35^{+0.18}_{-0.28}$				
HeLMS-42							
LURGS J00034.2+024114	$3.2^{+0.2}_{-0.2}$	3.30	$13.26^{+0.04}_{-0.05}$	LURGS J000319.2+02371 ^b
SGP-93302							
LURGS J000624.4–323018	$3.7^{+0.2}_{-0.2}$	0.14	$13.41^{+0.03}_{-0.03}$	LURGS J00067.7–322638	$4.4^{+0.2}_{-0.2}$	0.02	$13.45^{+0.04}_{-0.03}$
LURGS J000621.3–32328	$3.6^{+0.4}_{-0.3}$	0.26	$13.02^{+0.08}_{-0.06}$	LURGS J000619.9–323126	$2.2^{+0.4}_{-0.4}$	0.64	$12.50^{+0.12}_{-0.15}$
LURGS J00066.1–323016	$1.8^{+0.4}_{-0.5}$	1.05	$12.58^{+0.17}_{-0.29}$	LURGS J000619.9–322847	$1.9^{+0.4}_{-0.4}$	0.42	$12.43^{+0.14}_{-0.18}$
LURGS J000634.0–323138	$2.3^{+0.8}_{-0.7}$	0.13	$12.33^{+0.22}_{-0.28}$	LURGS J00068.5–323338 ^b
ELAISS1-18							
LURGS J002851.3–431353	$2.9^{+0.2}_{-0.2}$	0.87	$13.03^{+0.05}_{-0.06}$	LURGS J00297.7–431036	$2.8^{+0.2}_{-0.2}$	0.81	$13.05^{+0.06}_{-0.07}$
LURGS J002913.4–43077	$6.3^{+3.7}_{-4.1}$	1.38	$12.87^{+0.28}_{-0.71}$	LURGS J00294.0–430737	$1.4^{+1.1}_{-1.4}$	0.37	$12.08^{+0.44}_{-0.44}$
LURGS J002919.0–430817	$6.3^{+3.7}_{-4.1}$	0.75	$12.52^{+0.29}_{-0.76}$				
ELAISS1-26							
LURGS J003352.4–452015	$2.8^{+0.3}_{-0.3}$	2.47	$12.88^{+0.07}_{-0.08}$	LURGS J003410.4–452230	$2.2^{+0.4}_{-0.5}$	1.44	$12.83^{+0.13}_{-0.18}$
LURGS J003347.9–451441	$2.9^{+0.7}_{-0.7}$	0.16	$12.60^{+0.15}_{-0.20}$				
SGP-208073							
LURGS J003533.9–280260	$3.6^{+0.3}_{-0.2}$	0.96	$13.19^{+0.05}_{-0.05}$	LURGS J003540.1–280459	$2.7^{+0.3}_{-0.3}$	0.64	$12.92^{+0.08}_{-0.09}$
LURGS J003536.4–280143	$2.5^{+0.6}_{-0.6}$	1.25	$12.50^{+0.16}_{-0.20}$				
ELAISS1-29							
LURGS J003756.6–421519	$2.8^{+0.2}_{-0.3}$	3.89	$12.87^{+0.06}_{-0.07}$	LURGS J003831.5–421418 ^b
LURGS J003744.9–421240	$2.0^{+0.3}_{-0.3}$	1.15	$12.70^{+0.10}_{-0.12}$	LURGS J003811.7–42198 ^b
LURGS J003825.5–42128	$0.9^{+0.5}_{-0.7}$	0.34	$12.34^{+0.35}_{-1.29}$	LURGS J00388.4–421742	$2.3^{+0.3}_{-0.3}$	1.66	$12.64^{+0.10}_{-0.13}$
SGP-354388							
LURGS J004223.7–334325	$4.2^{+0.2}_{-0.2}$	0.19	$13.37^{+0.04}_{-0.03}$	LURGS J004223.5–334350	$3.5^{+0.3}_{-0.3}$	0.18	$13.15^{+0.06}_{-0.06}$
LURGS J004233.2–33444	$3.7^{+0.9}_{-0.5}$	0.36	$12.85^{+0.15}_{-0.11}$	LURGS J004223.2–334117	$3.2^{+0.6}_{-0.5}$	1.09	$12.81^{+0.12}_{-0.11}$
LURGS J004216.1–334138	$1.8^{+0.2}_{-0.2}$	0.06	$12.77^{+0.07}_{-0.09}$	LURGS J004219.8–334435	$2.6^{+0.3}_{-0.3}$	2.39	$12.72^{+0.08}_{-0.09}$
LURGS J004212.9–334544 ^b	LURGS J004210.1–334040 ^b
LURGS J004228.5–334925 ^b				
SGP-380990							
LURGS J004614.6–321828	$2.8^{+0.2}_{-0.2}$	4.55	$12.88^{+0.06}_{-0.06}$	LURGS J004620.2–32209	$2.7^{+0.3}_{-0.3}$	1.34	$12.77^{+0.09}_{-0.10}$
LURGS J00464.4–321844	$2.0^{+0.7}_{-1.0}$	0.23	$12.43^{+0.24}_{-0.55}$				
HeLMS-10							
LURGS J005258.6+061318	$3.2^{+0.1}_{-0.2}$	3.56	$13.48^{+0.03}_{-0.04}$	LURGS J00532.4+061113 ^b
LURGS J005310.4+061510	$2.5^{+0.2}_{-0.5}$	0.12	$12.97^{+0.13}_{-0.18}$				
SGP-221606							
LURGS J011918.9–294516	$2.8^{+0.2}_{-0.2}$	1.59	$13.04^{+0.06}_{-0.07}$	LURGS J011915.9–294748	$4.4^{+1.7}_{-1.2}$	2.72	$12.65^{+0.22}_{-0.22}$
LURGS J01191.8–294342	$1.3^{+3.7}_{-1.3}$	0.56	$11.71^{+0.99}_{-0.99}$	LURGS J01199.6–294241 ^b
SGP-146631							
LURGS J013155.8–311147	$2.9^{+0.3}_{-0.3}$	2.26	$12.89^{+0.08}_{-0.09}$	LURGS J01324.5–311239	$2.4^{+0.2}_{-0.2}$	20.97	$13.03^{+0.05}_{-0.06}$
LURGS J013215.5–310837 ^b				
SGP-278539							
LURGS J01428.2–323426	$2.9^{+0.3}_{-0.3}$	4.62	$12.94^{+0.07}_{-0.08}$	LURGS J014226.2–323324 ^b
LURGS J01421.6–323624	$5.2^{+4.1}_{-1.4}$	0.23	$12.91^{+0.37}_{-0.21}$	LURGS J014214.4–32290	$3.8^{+2.5}_{-1.6}$	0.06	$12.63^{+0.34}_{-0.41}$
LURGS J014218.2–32352 ^b				
SGP-142679							
LURGS J014456.9–284146	$2.7^{+0.2}_{-0.2}$	15.33	$13.03^{+0.05}_{-0.06}$	LURGS J014448.8–283535	$7.3^{+2.7}_{-2.2}$	2.69	$12.96^{+0.19}_{-0.23}$
LURGS J01456.7–284457	$2.1^{+0.1}_{-0.1}$	8.07	$13.12^{+0.05}_{-0.06}$				
XMM-15							
LURGS J021745.3–030912	$3.7^{+0.5}_{-0.5}$	0.01	$13.00^{+0.09}_{-0.09}$	LURGS J021757.1–030753	$1.2^{+0.4}_{-0.5}$	0.09	$12.51^{+0.23}_{-0.43}$
LURGS J021737.3–03128 ^b				
XMM-30							
LURGS J022656.6–032711	$3.5^{+0.2}_{-0.2}$	3.23	$13.19^{+0.03}_{-0.03}$	LURGS J022644.9–032510	$2.8^{+0.2}_{-0.1}$	3.05	$13.13^{+0.04}_{-0.04}$
LURGS J022630.2–032530	$2.9^{+0.7}_{-0.6}$	1.45	$12.84^{+0.15}_{-0.18}$	LURGS J02270.8–032541	$2.5^{+0.8}_{-0.9}$	0.53	$12.32^{+0.20}_{-0.32}$
LURGS J022650.0–032542	$1.8^{+0.4}_{-0.4}$	0.70	$12.47^{+0.14}_{-0.21}$				

Table 4
(Continued)

ID	z_{phot}^a	χ^2	$\log_{10}(L_{\text{far-IR}})$ (L_{\odot})	ID	z_{phot}^a	χ^2	$\log_{10}(L_{\text{far-IR}})$ (L_{\odot})
CDFS-13							
LURGS J03370.7–292148	3.0^{+0.2}_{-0.2}	1.51	13.21^{+0.05}_{-0.05}	LURGS J03370.3–291746	3.0 ^{+2.3} _{-0.8}	13.23	12.83 ^{+0.40} _{-0.25}
LURGS J033655.2–292627	2.6 ^{+1.1} _{-1.1}	0.15	12.44 ^{+0.26} _{-0.47}				
ADFS-27							
LURGS J043657.0–543813	4.4^{+0.4}_{-0.3}	0.92	13.23^{+0.06}_{-0.06}	LURGS J043729.9–54365	4.0 ^{+0.7} _{-0.6}	0.80	13.02 ^{+0.12} _{-0.12}
LURGS J04374.7–543914 ^b	LURGS J043717.4–54356	2.7 ^{+0.5} _{-0.5}	1.90	12.63 ^{+0.11} _{-0.14}
LURGS J043717.5–543528	2.0 ^{+0.2} _{-0.2}	11.45	12.80 ^{+0.07} _{-0.09}	LURGS J04377.5–54341	1.9 ^{+0.4} _{-0.5}	0.05	12.57 ^{+0.17} _{-0.28}
LURGS J043649.4–54408	3.1 ^{+0.9} _{-0.8}	0.54	12.54 ^{+0.18} _{-0.23}				
ADFS-32							
LURGS J044410.1–534949	3.0^{+0.6}_{-0.6}	0.45	12.65^{+0.12}_{-0.15}	LURGS J04450.4–53496 ^b
G09-83808							
LURGS J090045.7+004124	4.5^{+0.4}_{-0.3}	0.23	13.25^{+0.05}_{-0.05}	LURGS J090032.8+004313	2.3 ^{+0.1} _{-0.1}	6.55	13.15 ^{+0.04} _{-0.05}
LURGS J090019.4+004016 ^b	LURGS J090057.3+00415	2.1 ^{+0.3} _{-0.3}	1.20	12.60 ^{+0.09} _{-0.11}
LURGS J090054.2+004343	1.9 ^{+0.5} _{-0.5}	1.16	12.34 ^{+0.16} _{-0.23}	LURGS J090057.1+004039	1.8 ^{+0.3} _{-0.3}	6.49	12.45 ^{+0.12} _{-0.17}
LURGS J090037.1+003624	1.8 ^{+0.2} _{-0.2}	2.45	12.83 ^{+0.07} _{-0.09}				
G15-82684							
LURGS J14506.3+015038	3.2 ^{+0.2} _{-0.2}	1.24	13.14 ^{+0.04} _{-0.05}	LURGS J145013.1+014810	3.5^{+0.3}_{-0.2}	0.05	13.07^{+0.05}_{-0.05}
LURGS J145012.1+015158	2.7 ^{+0.3} _{-0.3}	0.58	12.93 ^{+0.07} _{-0.08}	LURGS J145015.4+015237	3.2 ^{+0.3} _{-0.3}	0.83	12.94 ^{+0.07} _{-0.07}
LURGS J145025.7+015115	2.3 ^{+0.4} _{-0.4}	0.83	12.62 ^{+0.11} _{-0.14}	LURGS J145023.8+01514	2.5 ^{+0.7} _{-0.7}	2.67	12.48 ^{+0.18} _{-0.25}
SGP-433089							
LURGS J222737.4–333835	2.5^{+0.3}_{-0.2}	0.87	12.77^{+0.08}_{-0.08}	LURGS J222725.2–333920	2.4 ^{+0.3} _{-0.3}	0.14	12.83 ^{+0.09} _{-0.10}
LURGS J222747.9–333533	2.5 ^{+0.4} _{-0.3}	0.21	12.71 ^{+0.10} _{-0.10}	LURGS J222731.1–33404 ^b
LURGS J222733.7–333440	1.9 ^{+0.3} _{-0.3}	0.66	12.66 ^{+0.10} _{-0.12}	LURGS J222737.7–333727	1.5 ^{+0.2} _{-0.3}	0.81	12.57 ^{+0.12} _{-0.15}
LURGS J222730.4–333534	2.3 ^{+0.6} _{-0.5}	0.16	12.57 ^{+0.16} _{-0.19}	LURGS J222750.1–334153	3.1 ^{+1.0} _{-0.7}	0.51	12.56 ^{+0.19} _{-0.18}
LURGS J222753.8–333529	2.6 ^{+0.5} _{-0.4}	4.51	12.58 ^{+0.13} _{-0.14}	LURGS J222727.8–334056	2.2 ^{+0.4} _{-0.4}	1.43	12.52 ^{+0.13} _{-0.15}
LURGS J222744.7–333741	2.3 ^{+0.4} _{-0.4}	6.69	12.49 ^{+0.13} _{-0.13}				

Notes.

^a We quote errors based on the $\chi^2 + 1$ values, without the adding the intrinsic template scatter in quadrature.

^b SPIRE non-detections for which we do not provide any photometric redshifts; we do not include these in our analysis.

emission—has a low probability of being ultra-red. We recall that this is shown in Table 3 and Figure 9, where galaxies with a higher probability of being ultra-red, which are thus more distant, primarily contribute to our overdensity parameter at $S' > 8.5$ mJy.

4.4. Physical Associations

To quantify whether the galaxies responsible for the overdensity are associated with their signpost ultra-red galaxy—thus comprising a protocluster—we analyze their photometric redshifts.

The simplest analysis we could perform is to calculate the absolute difference between the photometric redshifts of our field galaxies, z_{field} , relative to their respective target ultra-red galaxy, z_{target} . We therefore define a parameter

$$|\Delta z| = |z_{\text{target}} - z_{\text{field}}| \quad (6)$$

in order to determine the fraction of galaxies that lie at or below some association threshold, $|\Delta z|_{\text{thresh}}$. Choosing such a threshold is complicated by the difficult task of determining photometric redshifts using far-IR photometry alone.

For example, if we were to account for the fraction $\phi = \delta / (1 + \delta) = 0.5^{+0.6}_{-0.4}$ of sources responsible for our overdensity, $\delta = 1.0^{+0.6}_{-0.5}$, at $S' > 8.5$ mJy we would require an association threshold $|\Delta z|_{\text{thresh}} \leq 0.65$ (see Figure 11). In other

words, we have an overdensity of $\delta = 1.0$, comprised of 24 DSFGs with deboosted flux densities $S > 8.5$ mJy. We therefore expect $\phi = 0.5$ (or 12) of these DSFGs to be responsible for this overdensity. We achieve this association if we arbitrarily set our threshold to $|\Delta z|_{\text{thresh}} \leq 0.65$, as shown in Figure 11, where we plot the fraction of sources responsible for an overdensity against our association threshold.

On the other hand, if we choose a threshold dependent on the median fitting errors for our targets and field galaxies, $|\Delta z|_{\text{thresh}} \leq ((\sigma_{z_{\text{target}}})^2_{1/2} + (\sigma_{z_{\text{field}}})^2_{1/2})^{1/2} = 0.52$, we are unable to account for $\approx 20\%$ of the galaxies responsible for the overdensity. Finally, if we were to include in quadrature the intrinsic scatter in our three templates to the median fitting errors, our association threshold would increase to $|\Delta z|_{\text{thresh}} \leq 0.93$. As can be seen in Figure 11, this threshold includes all of the galaxies responsible for the overdensity, but is likely contaminated by unassociated galaxies (15%).

Both the former and latter association thresholds are too large to make any reliable claim of association. We therefore compromise, knowingly missing some of the galaxies responsible for the overdensity, by choosing an association threshold, $|\Delta z|_{\text{thresh}} \leq 0.52$. We do this in order to increase the reliability of our further analysis of these potential protocluster systems. With this approach for our entire catalog, we find that half of our target ultra-red galaxies have at least one associated DSFG.

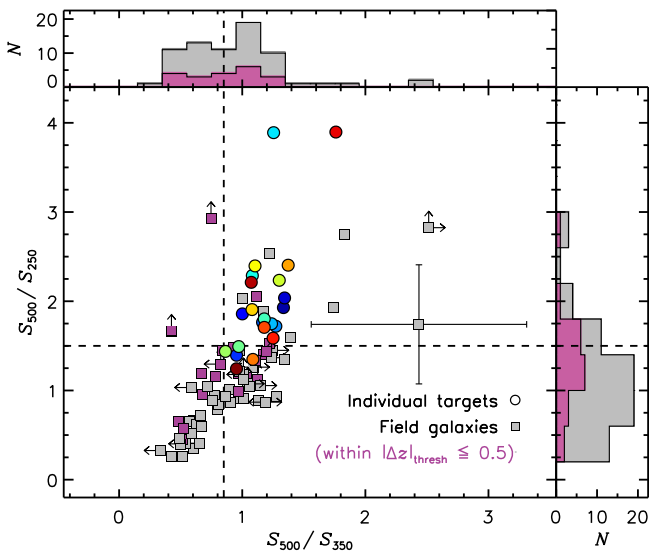


Figure 10. S_{500}/S_{350} vs. S_{500}/S_{250} for our catalog of sources that have at least one SPIRE detection above 1σ . We show our target (field) galaxies as circles (squares) and highlight in pink those field galaxies that lie within $|\Delta z| \leq 0.5$ of their signpost galaxy. We show our color-cut limits (dashed line), $S_{500}/S_{250} \geq 1.5$ and $S_{500}/S_{350} \geq 0.85$, which a target is required to match in order to meet our ultra-red galaxy selection criteria (i.e., the top right region of the plot). Five targets narrowly miss our S_{500}/S_{250} color-cut threshold, three by 0.1 and two by 0.2. This shift toward bluer colors is due to the larger $250\ \mu\text{m}$ boosting and the refined positions at which we make the SPIRE photometric measurements. A representative color uncertainty is shown, and we use arrows to highlight 1σ limits where applicable.

We illustrate the results of this analysis in the top panel of Figure 12, where we have chosen to plot Δz against the radial distance between field galaxies and their targets (Δr_{target}). Half of these associated DSFGs are within $\Delta r_{\text{target}} \lesssim 3'$ —suggesting that there is a slight dependence on association with proximity, in agreement with the annuli analysis of our number counts in Section 4.1. In terms of proper radial distances (derived at the redshift of the target), we see that these galaxies are distributed on scales of $\Delta r_{\text{target}} \sim 2$ Mpc, reporting an average separation of $\overline{\Delta r_{\text{target}}} = 1.6 \pm 0.5$ Mpc with an interquartile range $\Delta r_{\text{target}} = 1.0\text{--}2.2$ Mpc. We see no dependence on the redshift of the target ultra-red galaxy and the average target separation from $z = 2\text{--}4$.

The top panel of Figure 12 also shows that the majority of our field galaxies are at a lower redshift than their respective signpost galaxy, with the former lying at a median photometric redshift, $z_{1/2} = 2.6 \pm 0.2$, with interquartile range, $z = 1.9\text{--}3.1$, and the latter (our signposts) lying at a slightly higher redshift, $z_{1/2} = 3.2 \pm 0.2$, with an interquartile range, $z = 2.8\text{--}3.6$. If we remove the associated DSFGs, we refine the median photometric redshift for the “interloper” galaxies to be $z_{1/2} = 2.3 \pm 0.1$ with an interquartile range, $z = 1.8\text{--}2.8$, in good agreement with the general DSFG population (Chapman et al. 2005; Simpson et al. 2014).

Our associated DSFGs have a median rest-frame luminosity, $(L_{\text{far-IR}})_{1/2} = 10^{12.7} L_{\odot}$, with an interquartile range, $L_{\text{far-IR}} = 10^{12.6}\text{--}10^{12.9} L_{\odot}$. Between shells of proper radial distance from the target of $\Delta r_{\text{target}} = 0.3\text{--}1.3$ Mpc and $2.3\text{--}3.3$ Mpc, we see an average difference in luminosity of $\Delta L_{\text{far-IR}} = (3 \pm 2) \times 10^{12} L_{\odot}$. This slight increase in luminosity perhaps hints at the existence of a mechanism able to enhance the SF in denser environments (e.g., Oteo et al. 2017a).

We translate rest-frame luminosities into SFRs using $\psi/M_{\odot}\ \text{yr}^{-1} \approx 1.7 \times 10^{10} L_{\text{far-IR}}/L_{\odot}$ (see Equation (4) in Kennicutt, 1998, for starbursts using a Salpeter initial mass function (IMF), noting that a top-heavy IMF in distant dusty starbursts has been suggested many times—Romano et al. 2017). Hence, these associated galaxies have high median SFRs, $\psi_{1/2} = 1000 \pm 200 M_{\odot}\ \text{yr}^{-1}$, with an average total SFR, $\Psi = \Sigma\psi = 2200 \pm 500 M_{\odot}\ \text{yr}^{-1}$. This is consistent with a scenario wherein these galaxies form the bulk of their stellar mass quickly (in <1 Gyr) at $z \sim 3$ and evolve to populate the centers of massive galaxy clusters seen today (Thomas et al. 2005, 2010; Fassbender et al. 2011; Snyder et al. 2012).

To test the validity of this simplistic method for protocluster association, we calculate the same residual parameter, but this time for all galaxy pairs i and j in each map k , i.e., $|\Delta z_{i,j}|_k = |z_i - z_j|_k$, $\forall j > i$. We compare the average value of this parameter for all maps to that of a control sample. We determine the latter by replacing all galaxies except for our targets with a random galaxy drawn from the ALESS photometric redshift distribution presented in Simpson et al. (2014).

This alternative analysis is shown in the bottom panel of Figure 12, where we see a similar excess of $\phi \approx 0.3$ to that found in the previous analysis. Furthermore, this analysis shows that there is a deficit of $|\Delta z| \geq 1$ pairs, indicating that our field galaxies are preferentially associated with their target galaxies below this level. This alternative analysis, however, does not tell us which field galaxies are associated with the signpost ultra-red galaxies.

The similarities between the findings of both methods suggests that we can trust our analysis.

4.5. Consequent Fate at $z \sim 0$

Here, we briefly discuss the eventual fate of the ultra-red galaxy environments that have at least one DSFG associated with their signpost.

To recapitulate, just over half of our sample have at least one associated DSFG within $\Delta z \leq 0.52$. We have shown that these galaxies have high SFRs, with the candidate protoclusters themselves having an average total SFR of $\Psi \sim 2 \times 10^3 M_{\odot}\ \text{yr}^{-1}$. This supports a scenario wherein these galaxies evolve from $z \sim 3$ to the present to populate the centers of the most massive galaxy clusters seen in the local universe.

We now derive molecular gas masses, M_{H_2} , using the far-IR continuum and an appropriate scaling constant (α —Scoville et al. 2014, 2015), determined from a sample of 28 SMGs with CO(1–0) measurements at $z < 3$

$$\alpha = \frac{L_{850\ \mu\text{m}}}{M_{\text{H}_2}} = 1.0 \pm 0.5 \times 10^{20} \text{ erg s}^{-1} \text{ Hz } M_{\odot}^{-1}, \quad (7)$$

where $L_{850\ \mu\text{m}}$ is the rest-frame luminosity at $850\ \mu\text{m}$ determined from our best-fitting SEDs. We derive median gas masses, $(M_{\text{H}_2})_{1/2} = 1.7 \times 10^{11} M_{\odot}$, with an interquartile range, $M_{\text{H}_2} = 9.5 \times 10^{10}\text{--}2.1 \times 10^{11} M_{\odot}$, for our signpost ultra-red galaxies and their associated DSFGs. Thus, if each DSFG converts its reservoir of gas into stars, each would evolve into a present-day galaxy with an average total stellar mass of at least $\overline{M}_{\text{stars}} \gtrsim 10^{11} M_{\odot}$. Furthermore, we note that our signpost ultra-red galaxies have slightly elevated average gas masses of $\overline{M}_{\text{H}_2} = (2.5 \pm 1.2) \times 10^{11} M_{\odot}$ compared to their

Table 5
Signpost Galaxies and Their Photometric Properties

IAU Name	α (J2000) δ		S_{250}^b (mJy beam $^{-1}$)	S_{350}^b (mJy beam $^{-1}$)	S_{500}^b (mJy beam $^{-1}$)	S_{870}^b (mJy)	B	\mathcal{F}
	(h m s)	($^{\circ}$ ' ")						
SGP-28124								
LURGS J000124.9–354212	00:01:24.88	–35:42:12.2	62.2 \pm 9.1	89.8 \pm 8.8	119.9 \pm 9.3	44.3 \pm 1.4	1.04	1.00
LURGS J000145.0–353822	00:01:44.95	–35:38:22.1	55.9 \pm 7.9	67.4 \pm 8.6	52.4 \pm 9.4	15.9 \pm 2.6	1.15	1.00
LURGS J00014.2–354123	00:01:04.20	–35:41:23.0	5.9 \pm 7.5	11.7 \pm 8.8	4.7 \pm 9.7	6.4 \pm 1.5	1.35	0.97
LURGS J000122.9–354211	00:01:22.91	–35:42:11.2	31.9 \pm 9.0	47.9 \pm 8.7	87.8 \pm 9.4	10.2 \pm 1.4	1.11	0.92
LURGS J000138.5–35442	00:01:38.50	–35:44:02.3	4.0 \pm 9.2	9.2 \pm 9.2	–3.6 \pm 10.3	4.7 \pm 1.2	1.55	0.85
LURGS J000115.9–35411	00:01:15.90	–35:41:01.3	28.4 \pm 8.1	27.4 \pm 8.6	6.2 \pm 9.3	4.4 \pm 1.2	1.59	0.85
LURGS J000129.4–354416	00:01:29.39	–35:44:15.7	30.0 \pm 9.6	23.6 \pm 9.0	26.7 \pm 10.2	3.5 \pm 1.2	1.65	0.57
HeLMS-42								
LURGS J00034.2+024114	00:03:04.17	+02:41:13.7	39.8 \pm 9.2	60.3 \pm 9.9	81.0 \pm 11.3	42.6 \pm 3.6	1.89	1.00
LURGS J000319.2+02371	00:03:19.16	+02:37:00.7	1.3 \pm 8.6	3.6 \pm 8.9	–1.1 \pm 11.0	24.5 \pm 6.5	5.06	0.87
SGP-93302								
LURGS J000624.4–323018	00:06:24.44	–32:30:17.7	32.1 \pm 7.1	59.6 \pm 8.3	59.6 \pm 8.9	32.0 \pm 1.3	1.03	1.00
LURGS J00067.7–322638	00:06:07.68	–32:26:38.0	24.0 \pm 7.7	49.7 \pm 9.3	60.9 \pm 9.1	32.4 \pm 1.9	1.03	1.00
LURGS J000621.3–32328	00:06:21.31	–32:32:07.9	15.8 \pm 7.5	27.3 \pm 7.8	22.9 \pm 8.5	13.3 \pm 1.1	1.05	1.00
LURGS J000619.9–323126	00:06:19.92	–32:31:26.2	23.2 \pm 7.6	21.6 \pm 8.0	21.2 \pm 8.4	5.3 \pm 1.2	1.43	0.99
LURGS J00066.1–323016	00:06:06.14	–32:30:16.1	40.1 \pm 7.2	23.2 \pm 8.8	13.9 \pm 8.7	7.3 \pm 1.7	1.48	0.96
LURGS J000619.9–322847	00:06:19.91	–32:28:46.8	23.7 \pm 7.8	23.3 \pm 8.5	18.6 \pm 8.8	4.7 \pm 1.2	1.57	0.85
LURGS J000634.0–323138	00:06:34.00	–32:31:38.1	11.8 \pm 7.2	10.7 \pm 7.7	10.8 \pm 8.1	4.0 \pm 1.0	1.67	0.75
LURGS J00068.5–323338	00:06:08.47	–32:33:38.2	6.7 \pm 7.4	6.3 \pm 8.1	5.3 \pm 8.0	5.7 \pm 1.7	1.79	0.61
ELAIS-S1-18								
LURGS J002851.3–431353	00:28:51.31	–43:13:52.8	33.4 \pm 5.7	48.8 \pm 7.0	46.5 \pm 7.3	17.8 \pm 2.9	1.44	1.00
LURGS J00297.7–431036	00:29:07.74	–43:10:36.2	35.7 \pm 5.6	43.5 \pm 6.6	42.4 \pm 7.4	18.9 \pm 3.4	1.66	1.00
LURGS J002913.4–43077	00:29:13.39	–43:07:07.0	6.7 \pm 5.1	–0.2 \pm 6.2	6.5 \pm 7.1	25.1 \pm 5.9	3.20	0.99
LURGS J00294.0–430737	00:29:03.95	–43:07:37.2	17.7 \pm 5.8	11.1 \pm 6.6	4.2 \pm 7.2	18.0 \pm 4.6	4.60	0.87
LURGS J002919.0–430817	00:29:19.01	–43:08:16.8	–1.6 \pm 5.3	–1.8 \pm 6.2	7.7 \pm 7.5	17.5 \pm 5.9	5.29	0.69
ELAIS-S1-26								
LURGS J003352.4–452015	00:33:52.39	–45:20:14.6	24.5 \pm 6.6	37.0 \pm 8.3	43.1 \pm 9.6	12.6 \pm 2.6	1.57	1.00
LURGS J003410.4–452230	00:34:10.40	–45:22:29.7	45.7 \pm 9.2	37.6 \pm 9.1	18.6 \pm 10.2	14.8 \pm 3.1	1.55	1.00
LURGS J003347.9–451441	00:33:47.86	–45:14:40.8	11.6 \pm 6.1	20.6 \pm 6.9	13.8 \pm 7.3	15.9 \pm 4.6	3.11	0.78
SGP-208073								
LURGS J003533.9–280260	00:35:33.90	–28:02:59.5	27.7 \pm 7.7	37.4 \pm 8.8	47.6 \pm 9.7	19.2 \pm 1.8	1.16	1.00
LURGS J003540.1–280459	00:35:40.07	–28:04:58.7	32.3 \pm 7.6	31.2 \pm 8.5	28.1 \pm 9.8	12.4 \pm 2.0	1.22	1.00
LURGS J003536.4–280143	00:35:36.37	–28:01:43.3	14.7 \pm 7.9	16.8 \pm 9.0	23.4 \pm 9.7	7.1 \pm 2.0	2.23	0.72
ELAIS-S1-29								
LURGS J003756.6–421519^b	00:37:56.62	–42:15:19.0	24.9 \pm 6.2	35.1 \pm 7.5	43.5 \pm 8.0	7.7 \pm 2.3
LURGS J003831.5–421418	00:38:31.49	–42:14:18.4	–2.3 \pm 5.7	1.8 \pm 6.6	–1.4 \pm 7.3	20.0 \pm 4.8	2.02	0.95
LURGS J003744.9–421240	00:37:44.90	–42:12:39.6	41.7 \pm 6.7	45.8 \pm 7.7	27.8 \pm 8.3	10.3 \pm 2.7	2.59	0.90
LURGS J003811.7–42198	00:38:11.74	–42:19:08.0	0.5 \pm 5.5	–0.5 \pm 6.1	0.2 \pm 7.2	16.4 \pm 4.3	2.73	0.87
LURGS J003825.5–42128	00:38:25.48	–42:12:08.1	59.5 \pm 6.0	29.6 \pm 6.9	15.3 \pm 8.0	15.7 \pm 4.5	3.14	0.78
LURGS J00388.4–421742	00:38:08.44	–42:17:41.7	23.8 \pm 5.7	33.7 \pm 6.4	22.8 \pm 7.7	9.3 \pm 2.7	3.22	0.72
SGP-354388								
LURGS J004223.7–334325	00:42:23.73	–33:43:25.0	15.4 \pm 8.6	47.6 \pm 8.8	59.7 \pm 9.8	34.3 \pm 1.2	1.04	1.00
LURGS J004223.5–334350	00:42:23.46	–33:43:49.6	23.4 \pm 8.5	35.3 \pm 8.9	33.8 \pm 9.9	17.5 \pm 1.2	1.05	1.00
LURGS J004233.2–33444	00:42:33.16	–33:44:04.2	12.8 \pm 8.1	14.3 \pm 8.9	14.8 \pm 9.5	9.4 \pm 1.2	1.09	1.00
LURGS J004223.2–334117	00:42:23.25	–33:41:16.9	18.8 \pm 8.0	13.8 \pm 9.0	17.6 \pm 9.6	8.7 \pm 1.2	1.11	1.00
LURGS J004216.1–334138	00:42:16.11	–33:41:37.8	63.5 \pm 8.2	56.3 \pm 9.2	28.9 \pm 9.7	7.9 \pm 1.2	1.13	1.00
LURGS J004219.8–334435	00:42:19.79	–33:44:35.2	16.8 \pm 8.7	34.0 \pm 8.9	34.1 \pm 10.0	7.2 \pm 1.2	1.16	1.00
LURGS J004212.9–334544	00:42:12.86	–33:45:43.5	5.5 \pm 8.6	8.7 \pm 9.0	3.8 \pm 10.3	5.5 \pm 1.2	1.30	0.99
LURGS J004210.1–334040	00:42:10.09	–33:40:40.0	1.8 \pm 8.6	–1.1 \pm 8.6	–9.0 \pm 9.6	4.9 \pm 1.4	1.57	0.75
LURGS J004228.5–334925	00:42:28.53	–33:49:24.6	–4.0 \pm 8.6	–1.1 \pm 9.2	–15.2 \pm 10.3	10.9 \pm 2.8	1.49	0.72
SGP-380990								
LURGS J004614.6–321828	00:46:14.55	–32:18:28.1	20.4 \pm 8.2	43.1 \pm 8.9	46.6 \pm 9.3	10.4 \pm 1.6	1.18	1.00
LURGS J004620.2–32209	00:46:20.19	–32:20:08.5	24.3 \pm 8.5	29.2 \pm 9.0	34.3 \pm 9.3	9.2 \pm 1.8	1.31	1.00
LURGS J00464.4–321844	00:46:04.41	–32:18:44.2	23.2 \pm 8.0	17.4 \pm 8.6	8.3 \pm 9.3	7.6 \pm 2.2	2.18	0.69
HeLMS-10								
LURGS J005258.6+061318	00:52:58.61	+06:13:18.2	68.9 \pm 11.5	105.4 \pm 11.2	124.3 \pm 11.7	81.7 \pm 4.7	2.19	1.00
LURGS J00532.4+061113	00:53:02.41	+06:11:12.9	7.3 \pm 9.8	–3.7 \pm 10.7	6.7 \pm 12.3	23.8 \pm 5.8	7.62	0.98
LURGS J005310.4+061510	00:53:10.40	+06:15:09.5	45.3 \pm 11.4	51.6 \pm 11.8	29.5 \pm 12.5	38.3 \pm 8.4	3.59	0.98
SGP-221606								
LURGS J011918.9–294516	01:19:18.93	–29:45:15.7	34.9 \pm 7.7	53.6 \pm 8.8	52.1 \pm 9.9	20.3 \pm 3.9	1.82	1.00
LURGS J011915.9–294748	01:19:15.86	–29:47:47.6	1.2 \pm 8.0	0.0 \pm 9.0	22.6 \pm 9.1	16.2 \pm 4.1	3.80	0.94
LURGS J01191.8–294342	01:19:01.83	–29:43:42.0	7.9 \pm 7.6	7.2 \pm 9.1	–3.1 \pm 9.9	17.9 \pm 5.5	5.92	0.69

Table 5
(Continued)

IAU Name	α (J2000) δ		S_{250}^b (mJy beam $^{-1}$)	S_{350}^b (mJy beam $^{-1}$)	S_{500}^b (mJy beam $^{-1}$)	S_{870}^b (mJy)	B	\mathcal{F}
	(h m s)	($^{\circ}$ ' ")						
LURGS J01199.6–294241	01:19:09.59	–29:42:40.6	-0.1 ± 7.7	-0.9 ± 9.6	0.5 ± 9.8	15.5 ± 4.6	5.87	0.61
			SGP-146631					
LURGS J013155.8–311147	01:31:55.82	–31:11:47.0	26.1 \pm 7.4	32.7 \pm 7.5	39.9 \pm 8.0	15.0 \pm 3.3	1.87	0.98
LURGS J01324.5–311239	01:32:04.46	–31:12:38.5	47.2 ± 7.9	78.7 ± 7.6	67.9 ± 8.5	11.5 ± 3.2	3.92	0.94
LURGS J013215.5–310837	01:32:15.51	–31:08:36.6	5.7 ± 8.5	8.6 ± 8.8	6.4 ± 9.4	14.9 ± 4.0	3.73	0.85
			SGP-278539					
LURGS J01428.2–323426^b	01:42:08.20	–32:34:26.3	22.7 \pm 8.3	39.0 \pm 9.2	50.7 \pm 9.5	8.7 \pm 2.8
LURGS J014226.2–323324	01:42:26.25	–32:33:23.8	7.0 ± 8.4	2.6 ± 8.5	8.2 ± 9.2	17.2 ± 3.2	1.40	1.00
LURGS J01421.6–323624	01:42:01.58	–32:36:23.8	6.7 ± 8.7	7.4 ± 9.0	9.3 ± 9.0	14.1 ± 2.9	1.49	0.99
LURGS J014214.4–32290	01:42:14.41	–32:29:00.2	6.1 ± 8.1	9.5 ± 8.6	8.6 ± 9.6	15.7 ± 4.2	2.83	0.92
LURGS J014218.2–32352	01:42:18.19	–32:35:01.5	-0.1 ± 8.3	-7.2 ± 8.7	-2.8 ± 9.2	9.6 ± 2.8	3.26	0.65
			SGP-142679					
LURGS J014456.9–284146	01:44:56.88	–28:41:46.0	29.9 \pm 8.1	65.0 \pm 9.8	71.7 \pm 9.9	12.9 \pm 2.8	1.59	1.00
LURGS J014448.8–283535	01:44:48.78	–28:35:35.4	7.5 ± 7.7	-9.0 ± 8.5	10.5 ± 8.9	18.3 ± 4.2	1.88	0.97
LURGS J01456.7–284457	01:45:06.66	–28:44:57.3	97.2 ± 8.5	101.8 ± 9.8	82.2 ± 9.8	15.6 ± 3.5	1.70	0.96
			XMM-LSS-15					
LURGS J021745.3–030912	02:17:45.30	–03:09:12.3	12.6 \pm 6.2	22.2 \pm 7.2	24.0 \pm 7.8	17.6 \pm 3.0	1.47	1.00
LURGS J021757.1–030753	02:17:57.12	–03:07:53.0	56.8 ± 6.5	34.5 ± 7.4	14.6 ± 7.6	11.5 ± 2.9	2.67	0.90
LURGS J021737.3–03128	02:17:37.29	–03:12:08.0	0.5 ± 6.7	-0.3 ± 7.5	4.6 ± 8.2	10.8 ± 3.2	3.55	0.69
			XMM-LSS-30					
LURGS J022656.6–032711	02:26:56.60	–03:27:11.1	25.6 \pm 6.3	44.8 \pm 7.0	61.6 \pm 7.1	23.3 \pm 2.0	1.16	1.00
LURGS J022644.9–032510	02:26:44.90	–03:25:10.1	44.2 ± 6.3	65.6 ± 6.8	63.9 ± 7.5	18.8 ± 2.6	1.23	1.00
LURGS J022630.2–032530	02:26:30.16	–03:25:30.0	20.7 ± 5.7	24.3 ± 7.0	18.4 ± 7.7	29.8 ± 6.4	2.04	0.97
LURGS J02270.8–032541	02:27:00.81	–03:25:41.0	10.3 ± 6.5	10.3 ± 7.1	13.9 ± 7.8	7.6 ± 2.0	3.38	0.93
LURGS J022650.0–032542	02:26:50.00	–03:25:41.9	28.9 ± 6.5	28.6 ± 6.7	18.0 ± 7.3	7.6 ± 2.1	3.53	0.61
			CDFS-13					
LURGS J03370.7–292148	03:37:00.72	–29:21:48.0	41.1 \pm 5.9	51.0 \pm 7.1	55.4 \pm 7.2	26.2 \pm 3.5	1.45	1.00
LURGS J03370.3–291746	03:37:00.35	–29:17:45.8	23.3 ± 5.8	20.6 ± 6.8	10.5 ± 6.8	37.6 ± 5.9	1.45	1.00
LURGS J033655.2–292627	03:36:55.23	–29:26:26.9	11.6 ± 7.3	15.7 ± 7.3	7.6 ± 7.0	17.8 ± 5.0	5.46	0.75
			ADF-S-27					
LURGS J043657.0–543813	04:36:57.01	–54:38:13.2	16.5 \pm 6.0	24.0 \pm 7.1	28.2 \pm 7.8	25.3 \pm 1.8	1.24	1.00
LURGS J043729.9–54365	04:37:29.90	–54:36:04.5	14.9 ± 6.8	17.9 ± 7.9	19.9 ± 7.7	18.0 ± 3.3	1.34	1.00
LURGS J04374.7–543914	04:37:04.65	–54:39:13.7	3.7 ± 6.0	2.4 ± 8.0	0.4 ± 7.8	10.2 ± 1.9	1.35	1.00
LURGS J043717.4–54356	04:37:17.35	–54:35:06.2	13.5 ± 7.1	21.7 ± 7.9	25.5 ± 7.6	8.8 ± 2.4	2.35	0.98
LURGS J043717.5–543528	04:37:17.49	–54:35:28.3	48.7 ± 7.1	54.5 ± 7.8	49.0 ± 7.6	6.2 ± 2.3	2.59	0.93
LURGS J04377.5–54341	04:37:07.51	–54:34:00.6	34.2 ± 6.6	27.3 ± 7.9	13.6 ± 7.9	8.9 ± 2.3	2.18	0.93
LURGS J043649.4–54408	04:36:49.44	–54:40:08.4	7.9 ± 5.4	13.9 ± 6.9	5.2 ± 8.2	9.0 ± 2.2	2.00	0.78
			ADF-S-32					
LURGS J044410.1–534949^b	04:44:10.13	–53:49:49.1	13.1 \pm 6.0	16.6 \pm 6.8	20.8 \pm 8.0	5.5 \pm 2.8
LURGS J04450.4–53496	04:45:00.43	–53:49:06.2	9.3 ± 5.6	0.9 ± 6.8	-0.6 ± 8.0	20.0 ± 6.0	3.81	0.78
			G09-83808					
LURGS J090045.7+004124	09:00:45.74	+00:41:24.1	10.9 \pm 7.5	24.1 \pm 8.3	42.4 \pm 8.7	26.3 \pm 1.3	1.06	1.00
LURGS J090032.8+004313	09:00:32.77	+00:43:13.0	79.5 ± 6.6	69.2 ± 7.7	40.9 ± 8.1	18.5 ± 1.4	1.06	1.00
LURGS J090019.4+004016	09:00:19.37	+00:40:15.7	5.6 ± 6.4	-2.3 ± 7.4	-8.1 ± 7.3	18.3 ± 3.3	1.18	1.00
LURGS J090057.3+00415	09:00:57.28	+00:41:04.8	30.1 ± 7.3	32.5 ± 8.2	28.1 ± 9.0	5.5 ± 1.1	1.25	1.00
LURGS J090054.2+004343	09:00:54.21	+00:43:43.1	19.2 ± 7.5	18.8 ± 8.2	19.9 ± 8.9	3.7 ± 1.1	1.66	0.75
LURGS J090057.1+004039	09:00:57.08	+00:40:39.4	26.9 ± 7.4	33.6 ± 8.4	32.7 ± 9.0	3.2 ± 1.2	1.66	0.61
LURGS J090037.1+003624	09:00:37.14	+00:36:24.3	72.9 ± 6.6	65.4 ± 7.4	43.8 ± 8.3	8.6 ± 2.4	1.60	0.61
			G15-82684					
LURGS J14506.3+015038	14:50:06.29	+01:50:38.4	31.5 \pm 7.1	37.9 \pm 7.4	45.4 \pm 8.9	17.4 \pm 1.5	1.07	1.00
LURGS J145013.1+014810	14:50:13.10	+01:48:09.8	17.7 ± 7.5	36.4 ± 8.1	39.0 ± 9.2	17.2 ± 1.5	1.08	1.00
LURGS J145012.1+015158	14:50:12.06	+01:51:57.5	30.5 ± 7.3	34.0 ± 7.2	34.4 ± 8.7	11.2 ± 1.8	1.17	1.00
LURGS J145015.4+015237	14:50:15.43	+01:52:37.1	18.5 ± 7.3	33.9 ± 7.6	37.9 ± 8.5	13.2 ± 2.3	1.21	1.00
LURGS J145025.7+015115	14:50:25.66	+01:51:14.8	21.9 ± 7.8	31.7 ± 7.7	22.8 ± 9.1	7.1 ± 1.9	1.68	1.00
LURGS J145023.8+01514	14:50:23.82	+01:51:04.4	13.7 ± 7.6	9.8 ± 7.7	23.9 ± 8.9	5.4 ± 1.7	1.92	0.92
			SGP-433089					
LURGS J222737.4–333835	22:27:37.37	–33:38:34.7	28.3 \pm 9.2	36.8 \pm 10.0	35.1 \pm 10.8	8.1 \pm 1.1	1.12	1.00
LURGS J222725.2–333920	22:27:25.22	–33:39:19.5	35.3 ± 9.4	38.8 ± 10.4	20.2 ± 11.3	8.1 ± 1.4	1.16	1.00
LURGS J222747.9–333533	22:27:47.89	–33:35:32.7	21.7 ± 9.4	32.0 ± 9.8	25.1 ± 10.9	7.5 ± 1.3	1.17	1.00
LURGS J222731.1–33404	22:27:31.09	–33:40:03.7	5.0 ± 9.1	-8.0 ± 10.4	-1.1 ± 11.1	6.3 ± 1.2	1.21	1.00
LURGS J222733.7–333440	22:27:33.67	–33:34:40.2	40.2 ± 9.7	43.8 ± 10.0	28.8 ± 10.7	6.4 ± 1.3	1.24	1.00
LURGS J222737.7–333727	22:27:37.70	–33:37:26.8	49.7 ± 9.5	47.2 ± 9.9	23.2 ± 10.5	5.1 ± 1.1	1.31	0.99
LURGS J222730.4–333534	22:27:30.44	–33:35:33.6	18.5 ± 9.5	18.8 ± 9.9	18.2 ± 11.0	5.5 ± 1.3	1.35	0.96

Table 5
(Continued)

IAU Name	α (J2000) δ		S_{250}^b (mJy beam $^{-1}$)	S_{350}^b (mJy beam $^{-1}$)	S_{500}^b (mJy beam $^{-1}$)	S_{870}^b (mJy)	\mathcal{B}	\mathcal{F}
	(h m s)	($^{\circ}$ ' ")						
LURGS J222750.1–334153	22:27:50.14	–33:41:53.2	10.3 ± 9.9	11.5 ± 10.3	19.9 ± 10.8	7.0 ± 1.8	1.50	0.93
LURGS J222753.8–333529	22:27:53.81	–33:35:28.5	4.3 ± 9.7	38.1 ± 10.2	16.2 ± 10.9	6.4 ± 1.7	1.55	0.90
LURGS J222727.8–334056	22:27:27.79	–33:40:56.3	17.5 ± 9.6	27.9 ± 10.5	25.9 ± 11.1	5.2 ± 1.3	1.44	0.85
LURGS J222744.7–333741	22:27:44.74	–33:37:40.8	5.5 ± 9.4	37.0 ± 9.9	27.6 ± 10.8	4.5 ± 1.1	1.46	0.75

Notes. Targets are listed in order of increasing R.A. and are highlighted in bold. Each source detected in a given field is subsequently listed in increasing order of detected S/N.

^a SPIRE flux densities have been boosted to reflect the radial offset of a LABOCA source. Additionally, 870 μ m flux densities have been deboosted.

^b Signpost ultra-red galaxies that are undetected. We report the peak flux density and rms values for these sources within a 45'' aperture centered on the telescope pointing position. We do not provide flux-boosting (\mathcal{B}) or fidelity (\mathcal{F}) values.

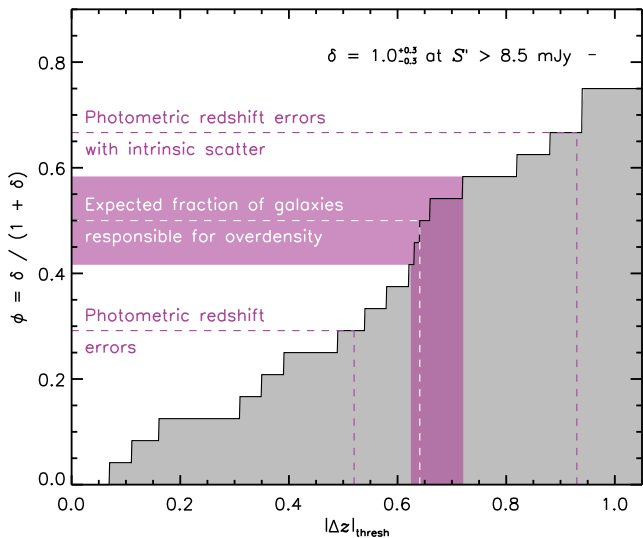


Figure 11. Fraction $\phi = \delta/(1 + \delta)$ of sources responsible for an overdensity (δ) as a function of association threshold, $|\Delta z|_{\text{thresh}}$. At $S' > 8.5$ mJy, we expect $\phi = 0.5^{+0.2}_{-0.2}$ of our bright DSFGs to be associated, which we only achieve if our threshold is set to $|\Delta z|_{\text{thresh}} \leq 0.65$. We also show that we overaccount or underaccount for DSFGs responsible for this overdensity if our threshold is based on the median photometric errors or is added in quadrature with the intrinsic template scatter. This motivates us to choose an association threshold of $|\Delta z|_{\text{thresh}} \approx 0.5$.

associated DSFGs. This is reminiscent of present-day massive cD ETGs, which dominate the centers of present-day galaxy clusters (Kelvin et al. 2014). However, we stress that without optical/near-IR imaging of these ultra-red galaxy environments, we are potentially missing many galaxies, each of which could contribute $M_{\text{stars}} \approx 10^9$ – $10^{11} M_{\odot}$ worth of stars to the final system (Overzier et al. 2009b; Casey et al. 2015); thus the possible stellar masses of these systems are largely unconstrained, and all these results should be regarded as firm lower limits.

Finally, we perform a crude space-density calculation of our ultra-red-galaxy-selected candidate protoclusters. We adjust the space-density redshift limits used for Equation (3) in Paper 1 to $2 \lesssim z \lesssim 6$ —motivated by the last epoch of virialized galaxy clusters (Casey 2016) and the highest of our ultra-red galaxy redshifts (Fudamoto et al. 2017; Zavala et al. 2017), respectively. We derive a space density of $\rho \sim 3 \times 10^{-6} \text{ Mpc}^{-3}$ for our ultra-red galaxies within $2 \lesssim z \lesssim 6$ assuming a star

formation lifetime of $t_{\text{burst}} = 100$ Myr. This roughly equates to the space density of $z < 0.5$ galaxy clusters with DM masses of $M_{\text{DM}} \sim 4 \times 10^{14} M_{\odot}$, i.e., so-called Virgo-type galaxy clusters (Bahcall & Cen 1993; Chiang et al. 2013). It should be noted, however, that perhaps only 20%–40% of all protoclusters within $2 \lesssim z \lesssim 6$ are actually rich in DSFG (Casey 2016).

However, as can be seen in the right-hand panel of Figures 6 and 9, not all of our ultra-red galaxies probe overdense regions. We estimate that only $33 \pm 8\%$ of our sample have overdensity parameters above $\delta(>8.5 \text{ mJy}) > 1$. Thus, we scale the space density of ultra-red galaxies accordingly to derive a proto-cluster space density of $\rho_{\text{proto-cluster}} \sim 9 \times 10^{-7} \text{ Mpc}^{-3}$.

4.6. Remarks on Selected Ultra-red Galaxies

We discuss some of the most exciting and/or overdense fields, each of which clearly warrants further exploration. We recall that the small areas and varying rms levels of each map mean that further analyses are heavily subject to the effects of cosmic variance.

1. *SGP-93302*. This is our deepest map, reaching an average beam-smoothed rms of $\bar{\sigma}_{870} = 1.7$ mJy. This 500 μ m riser has a deboosted flux density of $S_{870} = 30.9 \pm 1.3$ mJy. We estimate that this ultra-red galaxy lies at $z = 3.6^{+0.2}_{-0.1}$ and note that one (15%) of its field galaxies is an equally bright DSFG at $z = 3.4^{+0.4}_{-0.3}$ with a deboosted flux density of $S_{870} = 31.0 \pm 1.9$ mJy. This associated DSFG also meets our strict criteria of being an ultra-red galaxy. It is cataloged in Paper 1 as SGP-261206 and has been reported by Fudamoto et al. (2017) to lie at $z = 4.2$. Such an environment of robust ultra-red galaxies warrants spectroscopic follow-up and high-resolution imaging to explore the morphologies of its constituents. This map shows no particular overdensity or underdensity compared to LESS in the low flux-density regime, but it does show a 1σ excess at flux-density thresholds of $S' > 10$ mJy.
2. *SGP-354388*. This galaxy has been discussed by Oteo et al. (2017b). We revise the flux density of this extraordinary DSFG to $S_{870} = 33.0 \pm 1.2$ mJy, assuming that it can be deblended into two LABOCA point sources, separated by $\approx 25''$ as our extraction algorithm suggests. The multiplicitous nature of this source is also seen at higher resolutions, where ALMA 3mm continuum maps

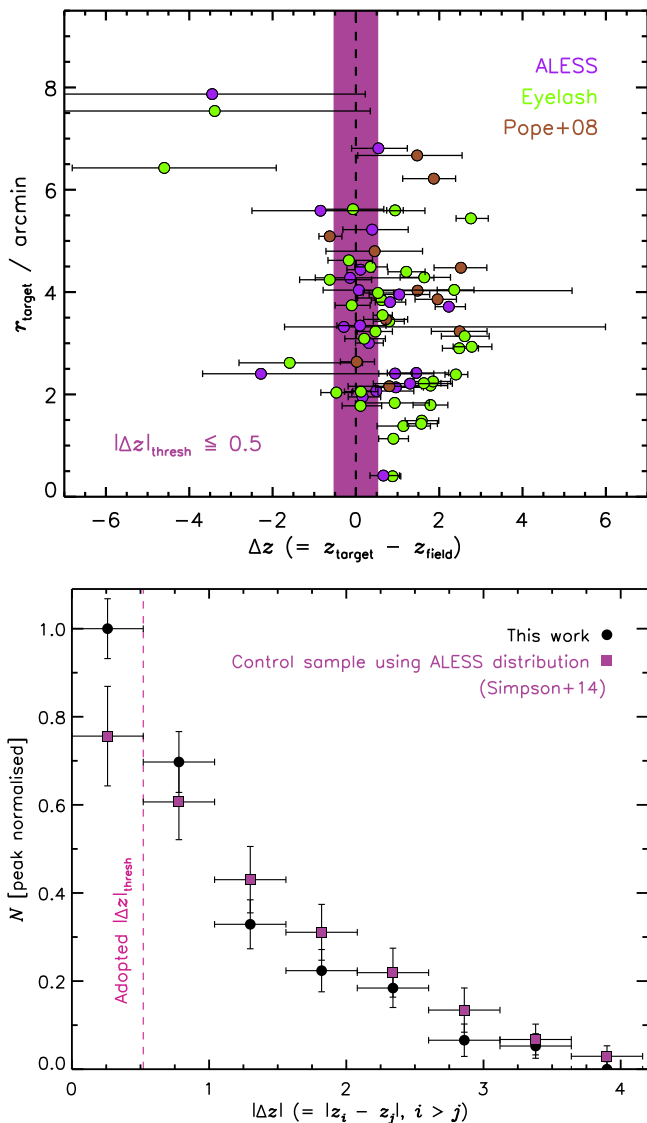


Figure 12. Top: Radial distance of our field galaxies to their signpost galaxies as a function of photometric redshift difference (Δz). Errors are deduced from the $\chi^2_{\min} + 1$ locations and are not added in quadrature with the intrinsic scatter. We note that the tail of sources with $\Delta z \geq 0$ reflects the fact that most galaxies are foreground to our targets, which sit at a median $z_{1/2} = 3.2$. The pink region indicates our threshold boundaries for association, in which a fraction $\phi \approx 0.3$ of our field galaxies lie. The large errors in our photometric redshifts highlight the difficulty of accurately constraining the redshifts of our DSFGs. Finally, we color-code each DSFG to indicate the best-fitting template adopted. Bottom: Alternative analysis of the absolute photometric redshift differences $|\Delta z_{i,j}|$ for all of our maps. We see a similar association excess to that of the top panel.

resolve the central fragments further, into three or more components (Oteo et al. 2017b). Like SGP-93302, this ultra-red galaxy only shows an overdensity of sources at flux-density thresholds $S' > 10$ mJy. We are only able to associate two of its nine field galaxies, although a further two DSFGs have unconstrained photometric redshifts. We refine its photometric redshift to $z = 4.2 \pm 0.2$ using improved SPIRE measurements made at the $870 \mu\text{m}$ position, which is consistent with its spectroscopic redshift, $z_{\text{spec}} = 4.002$ (Oteo et al. 2017a).

3. *SGP-433089*. This galaxy marks the most overdense field in our sample, which we place at a distance of

$z = 2.5 \pm 0.2$. We associate 6 of its 10 field galaxies with the signpost, noting that 1 of its field galaxies has an unconstrained photometric redshift. This map shows a deficit of bright DSFGs compared to the other maps explored here. Thus it does not contribute to our overdensity parameter at $S > 8.5$ mJy. Its brightest source (the signpost galaxy) has a deboosted flux density, $S_{870} = 7.2 \pm 1.1$ mJy, while the mean deboosted flux density of the detected field galaxies is $\bar{S}_{870} = 4.7$ mJy. The detection of these relatively faint DSFGs is due to the low average rms, $\bar{\sigma}_{870} = 1.1$ mJy, which allows us to report an overdensity factor of $\delta = 0.7^{+0.9}_{-0.6}$ at a flux density threshold of $S' > 4$ mJy.

4. *ADFS-27*. 3 mm scans with ALMA suggest that this ultra-red galaxy lies at $z \approx 5.7$ (Riechers et al. 2017)—drastically different to the estimate that we provide in this paper. Riechers et al. (2017) derive a dust temperature of $T_{\text{dust}} \approx 55$ K for this source, which highlights the strong degeneracy between temperature and redshift when using far-IR photometry alone to derive photometric redshifts. For instance, when we use a hotter but on average less accurate template for ultra-red galaxies (Paper I), such as HFLS 3, we revise the photometric redshift for this galaxy to $z_{\text{phot}} = 5.9^{+0.5}_{-0.4}$, i.e., to within 1σ of its reported spectroscopic value. This source has two associated DSFGs that lie within $\Delta z \approx 0.5$ —making it an ideal high-redshift candidate protocluster to follow up further. Finally, we note that our SPIRE flux densities are higher by ≈ 2 – 5 mJy than those presented in Riechers et al. (2017), i.e., from the *HerMES* xID250 catalog from which this source was originally selected. This is due to remeasuring these flux densities at the position of the LABOCA peak, resulting in photometry that makes *ADFS-27* appear less red.
5. *G09-83808*. This is a gravitationally lensed ($\mu \approx 9$) ultra-red galaxy, with a photometric redshift estimate that is also catastrophically lower than its spectroscopic value. Recent work by Zavala et al. (2017) shows that this galaxy resides at $z \sim 6$, rather than $z_{\text{phot}} = 4.45^{+0.4}_{-0.3}$ as presented here. Again, this DSFG highlights the temperature-redshift degeneracy because adopting HFLS 3 as a template yields a photometric redshift that is more consistent with its spectroscopic redshift, $z_{\text{phot}} = 6.2^{+0.5}_{-0.4}$.

4.7. Caveats

1. A larger sample of ultra-red galaxies would help to further reduce the effects of cosmic variance within our sample. We could improve our fidelity by achieving a uniform depth, comparable to that of SGP-93302, for example, so $\bar{\sigma} = 1.3$ mJy, for all existing ultra-red galaxies. This would reduce the number of potentially spurious LABOCA sources present in our catalog. A uniform, wide imaging survey would also allow the detection of less luminous DSFGs in the vicinity of our signposts, out to a radius of $\Delta R_{\text{target}} \approx 6'$.
2. The intrinsic luminosity of our associated DSFGs will depend on the gravitational lensing that each may have suffered. Although we have made an effort to avoid lensing in our selection of the signpost galaxies, as outlined in Paper I, a fraction of our ultra-red galaxies are gravitationally magnified by chance alignments

(Oteo et al. 2017b). Our SFRs, and average total SFRs, are thus upper limits, although the effect of invariant IMFs in these galaxies likely has a greater impact.

3. When we use the 850 μm number counts from S2CLS, our overdensity parameter rises to $\delta_{\text{S2CLS}} = 2.1_{-0.5}^{+0.6}$ at $S' > 8.5$ mJy. Although the errors remain similar (as they are dominated by the Poisson noise), we find that δ_{S2CLS} is $\gtrsim 2\sigma$ higher than that determined using LESS as a comparison.
4. Our association analysis likely underestimates the number of true physical associations. Our template fitting algorithm is accurate to only $\sigma_z = 0.14(1+z)$, typically much larger than the errors determined from the $\chi_{\text{min}}^2 + 1$ values at high redshift. Thus our fixed association threshold leads us to miss some associated DSFGs. Some galaxies not associated with a signpost galaxy will be falsely assigned until ALMA spectroscopy can improve upon the accuracy of our photometric redshifts.
5. Optical identification of the surrounding LBGs is necessary if we are to accurately constrain the total stellar mass—and thus DM component, and the eventual fate at $z \sim 0$ —of these protoclusters.

5. Conclusion

We have presented 870 μm imaging obtained with LABOCA on APEX for a sample of 22 ultra-red galaxies—12 and 10 from the *H-ATLAS* and *HerMES* imaging surveys, respectively—selected originally via their red *Herschel* 250, 350, and 500 μm flux-density ratios.

Our survey covers an area of $\mathcal{A} \approx 0.8 \text{ deg}^2$ down to an average rms depth of $\bar{\sigma} = 3.9 \text{ mJy beam}^{-1}$. Running our extraction algorithm at an S/N detection threshold of $\Sigma_{\text{thresh}} > 3.5$, we detect 86 field galaxies around our 22 ultra-red galaxies. We compute number counts and compare them to those reported in a comparable survey, LESS (Weiß et al. 2009). We report an overdensity factor (excluding our target ultra-red galaxies) of $\delta = 1.0_{-0.3}^{+0.5}$ at $S' > 8.5$ mJy. There exists a positive correlation between overdensity and 870 μm flux density, such that our sample of ultra-red galaxies traces dense regions, rich in brighter DSFGs.

We perform photometry on SPIRE maps at the positions of our LABOCA detections to derive photometric redshifts using three template SEDs. We find that our ultra-red galaxy sample has a median redshift $z_{1/2} = 3.2 \pm 0.2$, with interquartile range $z = 2.8\text{--}3.6$. We associate the field galaxies likely responsible for this overdensity to within $|\Delta z| \leq 0.65$ of their signpost ultra-red galaxy. Over half of our ultra-red galaxies have an average of one associated DSFG within $|\Delta z| \lesssim 0.5$. When these associated DSFGs are removed, the median redshift of the field galaxies decreases to $z_{1/2} = 2.3 \pm 0.1$, in line with the general DSFG population. The majority of the associated DSFGs are distributed on scales of $\overline{\Delta r}_{\text{target}} \sim 2 \text{ Mpc}$ from their signpost galaxy and have high median SFRs, $\psi_{1/2} \approx 1000 \pm 200 M_{\odot} \text{ yr}^{-1}$. We determine average total SFRs of $\overline{\Psi} = 2200 \pm 500 M_{\odot} \text{ yr}^{-1}$ for those systems with at

least one associated DSFG. We derive gas masses for our ultra-red galaxies and their associated DSFGs, determining average total stellar masses of $M_{\text{stars}} \sim 10^{11} M_{\odot}$ for these systems if they convert all of their gas into stars by $z \sim 0$. We determine an ultra-red galaxy protocluster space density of $\rho_{\text{proto-cluster}} \sim 9 \times 10^{-7} \text{ Mpc}^{-3}$ between $2 \lesssim z \lesssim 6$, which is similar to that of the most massive ($M_{\text{DM}} \sim 10^{15} M_{\odot}$) galaxy clusters at $z < 0.2$ (Bahcall & Cen 1993; Casey 2016; Overzier 2016). It therefore seems plausible that these systems of DSFGs may evolve into the massive ETGs that populate the centers of rich galaxy clusters at $z = 0$.

We have increased the number of potential distant DSFG protoclusters using our novel signposting technique, based on ultra-red SPIRE flux-density ratios. With deep optical imaging/spectroscopy of these environments, we will be able to better determine their ultimate stellar masses—and thus DM properties, enabling us to predict the eventual fate of these systems.

Our catalogs and 870 μm images form part of a formal data release.

A.J.R.L., R.J.I., J.M.S., I.O., L.D., V.A., and Z.Y.Z. acknowledge support from the European Research Council (ERC) in the form of Advanced Grant, 321302, COSMICISM.

H.D. acknowledges financial support from the Spanish Ministry of Economy and Competitiveness (MINECO) under the 2014 Ramón y Cajal program MINECO RYC-2014-15686. J.L.W. acknowledges support from an STFC Ernest Rutherford Fellowship. D.R. acknowledges support from the National Science Foundation under grant number AST-1614213. G.D.Z. acknowledges support from ASI/INAF agreement n. 2014-024-R.1. We pay special thanks to the useful feedback provided on the draft version of this work to D. Farrah, J. Greenslade, M. J. Michalowski, and I. Valtchanov. This research has made use of data from *HerMES* project (<http://hermes.sussex.ac.uk/>). *HerMES* is a *Herschel* Key Programme utilizing Guaranteed Time from the SPIRE instrument team, ESAC scientists and a mission scientist. The *H-ATLAS* is a project with *Herschel*, which is an ESA space observatory with science instruments provided by European-led Principal Investigator consortia and with important participation from NASA. The *H-ATLAS* website is <http://www.h-atlas.org>. US participants in *H-ATLAS* acknowledge support from NASA through a contract from JPL. This publication is based on data acquired with the Atacama Pathfinder Experiment (APEX). APEX is a collaboration between the Max-Planck-Institut für Radioastronomie, the European Southern Observatory, and the Onsala Space Observatory. Based on observations made with APEX under European Southern Observatory program E-191. A-0748 and Max Planck Institute (MPI) programs M-090.F-0025-2012, M-091.F-0021-2013 and M-092.F-0015-2013.

Facilities: APEX, *Herschel*.

Appendix A LABOCA and SPIRE maps

Here we present our LABOCA and *Herschel* imaging. The final S/N maps are shown in Figure 13.

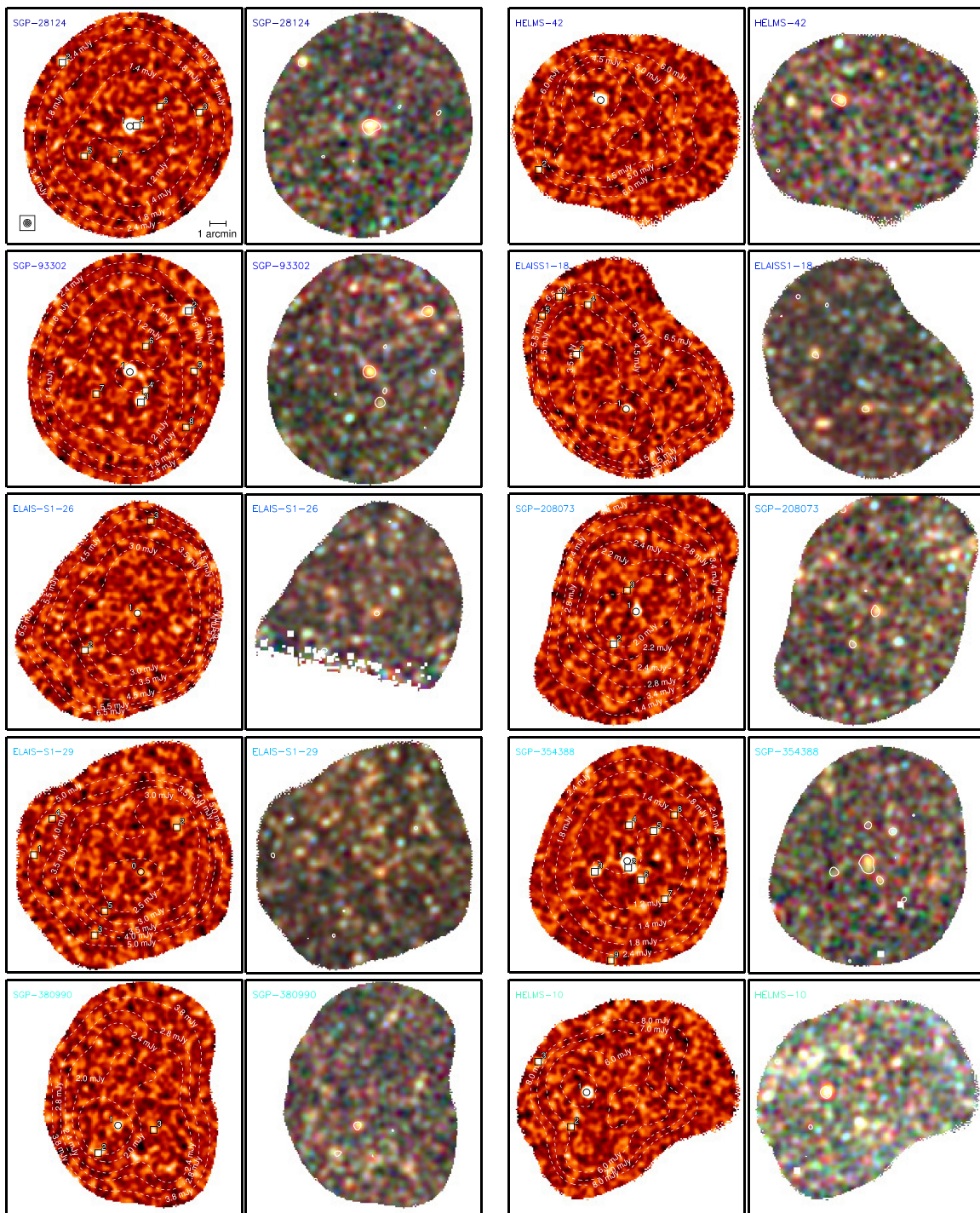


Figure 13. Left: $14' \times 14'$ cutouts of our LABOCA S/N maps at a spatial resolution of $\approx 27''$, stretched linearly between $\pm 3.5\sigma$ (see beam inset and scale in the top left panel). North is up; east is left. Detections above $\Sigma_{\text{thresh}} = 3.5$ are numbered in decreasing order of S/N, with hollow squares and stars representing signpost and field galaxies, respectively. Signposts numbered “0” are sources that we have been unable to detect above our 3.5σ threshold. We place dashed white contours at varying values of map noise. We show an arcminute scale and a LABOCA beam on the top row. Right: False-color, matched-filtered *Herschel* SPIRE $14' \times 14'$ cutout images, aligned with their LABOCA counterparts, which we use to measure the SPIRE photometry. White dashed contours are placed at LABOCA 3.5σ values. The maps are presented in increasing order of R.A., i.e., in the same order as they appear in Table 5, and their labels have been color-coded from blue to red.

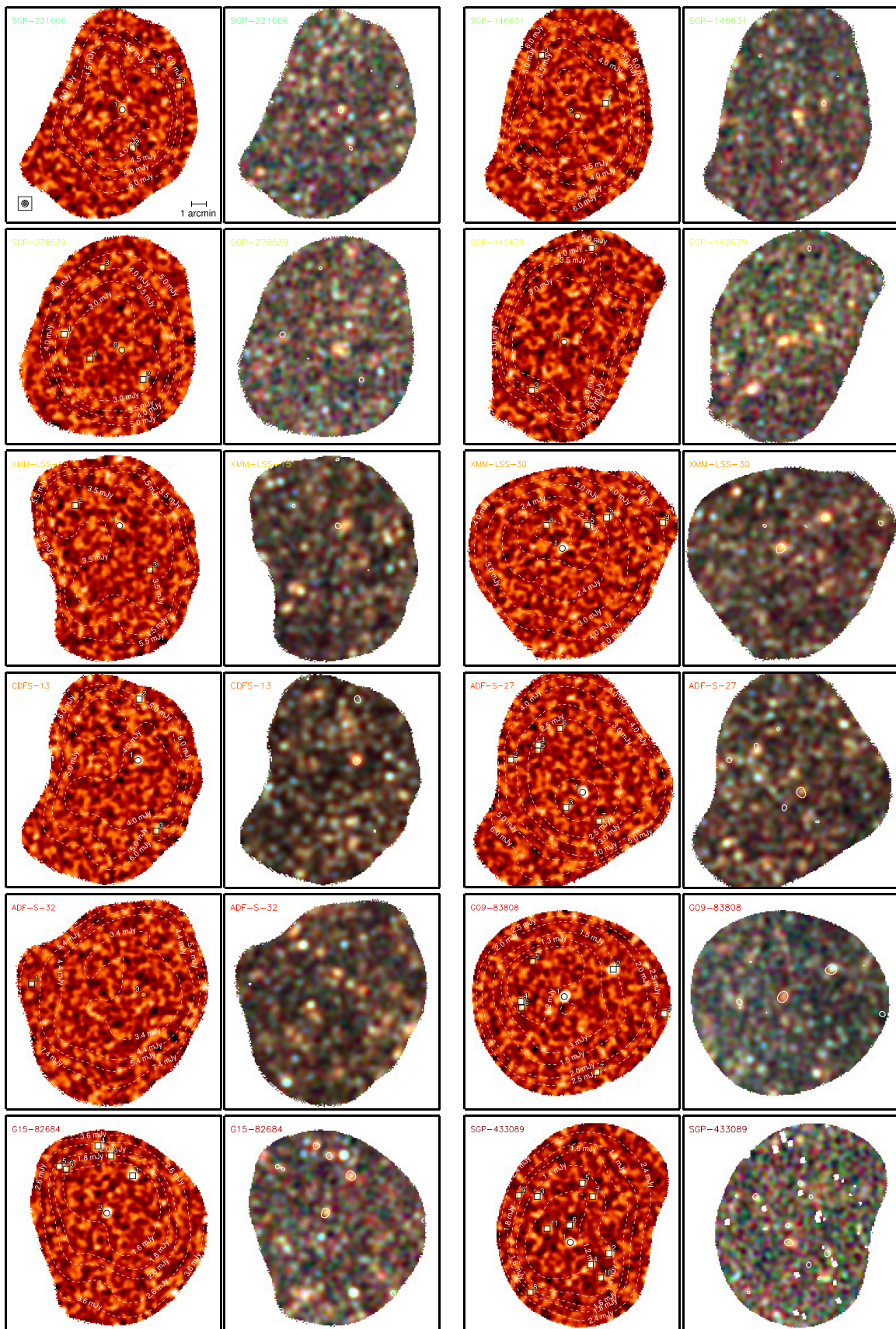














Figure 13. (Continued.)

ORCID iDs

A. J. R. Lewis  <https://orcid.org/0000-0002-2818-1478>
 R. J. Ivison  <https://orcid.org/0000-0001-5118-1313>
 A. Weiss  <https://orcid.org/0000-0003-4678-3939>
 I. Oteo  <https://orcid.org/0000-0001-5875-3388>
 D. L. Clements  <https://orcid.org/0000-0002-9548-5033>
 H. Dannerbauer  <https://orcid.org/0000-0001-7147-3575>
 S. Maddox  <https://orcid.org/0000-0001-5549-195X>
 S. J. Oliver  <https://orcid.org/0000-0001-7862-1032>
 A. Omont  <https://orcid.org/0000-0002-4721-3922>
 D. A. Riechers  <https://orcid.org/0000-0001-9585-1462>
 S. Serjeant  <https://orcid.org/0000-0002-0517-7943>
 J. Wardlow  <https://orcid.org/0000-0003-2376-8971>

References

- Aravena, M., Decarli, R., Walter, F., et al. 2016, *ApJ*, 833, 68
 Asboth, V., Conley, A., Sayers, J., et al. 2016, *MNRAS*, 462, 1989
 Bahcall, N. A., & Cen, R. 1993, *ApJL*, 407, L49
 Baldry, I. K., Glazebrook, K., Brinkmann, J., et al. 2004, *ApJ*, 600, 681
 Balogh, M. L., Navarro, J. F., & Morris, S. L. 2000, *ApJ*, 540, 113
 Barger, A. J., Wang, W.-H., Cowie, L. L., et al. 2012, *ApJ*, 761, 89
 Beelen, A., Omont, A., Bavouzet, N., et al. 2008, *A&A*, 485, 645
 Bell, E. F., Wolf, C., Meisenheimer, K., et al. 2004, *ApJ*, 608, 752
 Belloche, A., Schuller, F., Parise, B., et al. 2011, *A&A*, 527, A145
 Bernardi, M., Nichol, R. C., Sheth, R. K., Miller, C. J., & Brinkmann, J. 2006, *AJ*, 131, 1288
 Biggs, A. D., Ivison, R. J., Ibar, E., et al. 2011, *MNRAS*, 413, 2314
 Blain, A. W., Smail, I., Ivison, R. J., Kneib, J.-P., & Frayer, D. T. 2002, *PhR*, 369, 111
 Bourne, N., Dunne, L., Maddox, S. J., et al. 2016, *MNRAS*, 462, 1714
 Bower, R. G., Benson, A. J., Malbon, R., et al. 2006, *MNRAS*, 370, 645
 Bower, R. G., Kodama, T., & Terlevich, A. 1998, *MNRAS*, 299, 1193
 Busmann, R. S., Riechers, D., Fialkov, A., et al. 2015, *ApJ*, 812, 43
 Capak, P. L., Riechers, D., Scoville, N. Z., et al. 2011, *Natur*, 470, 233
 Casado, J., Ascasibar, Y., Gavilán, M., et al. 2015, *MNRAS*, 451, 888
 Casey, C. M. 2016, *ApJ*, 824, 36
 Casey, C. M., Chen, C.-C., Cowie, L. L., et al. 2013, *MNRAS*, 436, 1919
 Casey, C. M., Cooray, A., Capak, P., et al. 2015, *ApJL*, 808, L33
 Casey, C. M., Narayanan, D., & Cooray, A. 2014, *PhR*, 541, 45
 Chapman, S. C., Blain, A. W., Smail, I., & Ivison, R. J. 2005, *ApJ*, 622, 772
 Chiang, Y.-K., Overzier, R., & Gebhardt, K. 2013, *ApJ*, 779, 127
 Clements, D. L., Braglia, F., Pettipas, G., et al. 2016, *MNRAS*, 461, 1719
 Condon, J. J. 2007, in ASP Conf. Ser. 380, *Deepest Astronomical Surveys*, ed. J. Afonso et al. (San Francisco, CA: ASP), 189
 Conley, A., Cooray, A., Vieira, J. D., et al. 2011, *ApJL*, 732, L35
 Cooper, M. C., Tremonti, C. A., Newman, J. A., & Zabludoff, A. I. 2008, *MNRAS*, 390, 245
 Coppin, K., Chapin, E. L., Mortier, A. M. J., et al. 2006, *MNRAS*, 372, 1621
 Cowie, L. L., Songaila, A., Hu, E. M., & Cohen, J. G. 1996, *AJ*, 112, 839
 Dannerbauer, H., Kurk, J. D., De Breuck, C., et al. 2014, *A&A*, 570, A55
 Delahaye, A. G., Webb, T. M. A., Nantais, J., et al. 2017, *ApJ*, 843, 126
 Dowell, C. D., Conley, A., Glenn, J., et al. 2014, *ApJ*, 780, 75
 Dressler, A., Oemler, A., Jr., Couch, W. J., et al. 1997, *ApJ*, 490, 577
 Eales, S., Dunne, L., Clements, D., et al. 2010, *PASP*, 122, 499
 Elbaz, D., Daddi, E., Le Borgne, D., et al. 2007, *A&A*, 468, 33
 Fassbender, R., Nastasi, A., Böhringer, H., et al. 2011, *A&A*, 527, L10
 Fudamoto, Y., Ivison, R. J., Oteo, I., et al. 2017, *MNRAS*, 472, 2028
 Geach, J. E., Chapin, E. L., Coppin, K. E. K., et al. 2013, *MNRAS*, 432, 53
 Geach, J. E., Dunlop, J. S., Halpern, M., et al. 2017, *MNRAS*, 465, 1789
 Gehrels, N. 1986, *ApJ*, 303, 336
 Gerke, B. F., Newman, J. A., Faber, S. M., et al. 2007, *MNRAS*, 376, 1425
 Gomez, H. L., Vlahakis, C., Stretch, C. M., et al. 2010, *MNRAS*, 401, L48
 Granato, G. L., De Zotti, G., Silva, L., Bressan, A., & Danese, L. 2004, *ApJ*, 600, 580
 Greve, T. R., Ivison, R. J., Bertoldi, F., et al. 2004, *MNRAS*, 354, 779
 Griffin, M. J., Abergel, A., Abreu, A., et al. 2010, *A&A*, 518, L3
 Gunn, J. E., & Gott, J. R., III 1972, *ApJ*, 176, 1
 Hine, N. K., Geach, J. E., Alexander, D. M., et al. 2016, *MNRAS*, 455, 2363
 Hinshaw, G., Weiland, J. L., Hill, R. S., et al. 2009, *ApJS*, 180, 225
 Ivison, R. J., Dunlop, J. S., Smail, I., et al. 2000, *ApJ*, 542, 27
 Ivison, R. J., Greve, T. R., Dunlop, J. S., et al. 2007, *MNRAS*, 380, 199
 Ivison, R. J., Lewis, A. J. R., Weiss, A., et al. 2016, *ApJ*, 832, 78
 Ivison, R. J., Swinbank, A. M., Swinyard, B., et al. 2010, *A&A*, 518, L35
 Karim, A., Swinbank, A. M., Hodge, J. A., et al. 2013, *MNRAS*, 432, 2
 Kelvin, L. S., Driver, S. P., Robotham, A. S. G., et al. 2014, *MNRAS*, 444, 1647
 Kennicutt, R. C., Jr. 1998, *ARA&A*, 36, 189
 Kreysa, E., Bertoldi, F., Gemuend, H.-P., et al. 2003, *Proc. SPIE*, 4855, 41
 Lacey, C., & Cole, S. 1993, *MNRAS*, 262, 627
 Lacey, C. G., Baugh, C. M., Frenk, C. S., et al. 2016, *MNRAS*, 462, 3854
 Landsman, W. B. 1993, in ASP Conf. Ser. 52, *Astronomical Data Analysis Software and Systems II*, ed. R. J. Hanisch, R. J. V. Brissenden, & J. Barnes (San Francisco, CA: ASP), 246
 Larson, R. B., Tinsley, B. M., & Caldwell, C. N. 1980, *ApJ*, 237, 692
 Madau, P., Ferguson, H. C., Dickinson, M. E., et al. 1996, *MNRAS*, 283, 1388
 Miley, G. K., Overzier, R. A., Zirm, A. W., et al. 2006, *ApJL*, 650, L29
 Miller, T. B., Chapman, S. C., Hayward, C. C., et al. 2016, arXiv:1611.08552
 Miller, T. B., Hayward, C. C., Chapman, S. C., & Behroozi, P. S. 2015, *MNRAS*, 452, 878
 Morselli, L., Mignoli, M., Gilli, R., et al. 2014, *A&A*, 568, A1
 Muldrew, S. I., Hatch, N. A., & Cooke, E. A. 2015, *MNRAS*, 452, 2528
 Narayanan, D., Turk, M., Feldmann, R., et al. 2015, *Natur*, 525, 496
 Negrello, M., González-Nuevo, J., Magliocchetti, M., et al. 2005, *MNRAS*, 358, 869
 Negrello, M., Hopwood, R., De Zotti, G., et al. 2010, *Sci*, 330, 800
 Nelan, J. E., Smith, R. J., Hudson, M. J., et al. 2005, *ApJ*, 632, 137
 Nord, M., Basu, K., Pacaud, F., et al. 2009, *A&A*, 506, 623
 Oliver, S. J., Bock, J., Altieri, B., et al. 2012, *MNRAS*, 424, 1614
 Oteo, I., Ivison, R. J., Dunne, L., et al. 2017a, arXiv:1709.02809
 Oteo, I., Ivison, R. J., Negrello, M., et al. 2017b, arXiv:1709.04191
 Overzier, R. A. 2016, *A&ARv*, 24, 14
 Overzier, R. A., Guo, Q., Kauffmann, G., et al. 2009a, *MNRAS*, 394, 577
 Overzier, R. A., Shu, X., Zheng, W., et al. 2009b, *ApJ*, 704, 548
 Peebles, P. J. E., & Yu, J. T. 1970, *ApJ*, 162, 815
 Pilbratt, G. L., Riedinger, J. R., Passvogel, T., et al. 2010, *A&A*, 518, L1+
 Pope, A., Chary, R.-R., Alexander, D. M., et al. 2008, *ApJ*, 675, 1171
 Riechers, D. A., Bradford, C. M., Clements, D. L., et al. 2013, *Natur*, 496, 329
 Riechers, D. A., Leung, T. K. D., Ivison, R. J., et al. 2017, arXiv:1705.09660
 Rigby, E. E., Hatch, N. A., Röttgering, H. J. A., et al. 2014, *MNRAS*, 437, 1882
 Robertson, B., Li, Y., Cox, T. J., Hernquist, L., & Hopkins, P. F. 2007, *ApJ*, 667, 60
 Robson, E. I., Ivison, R. J., Smail, I., et al. 2014, *ApJ*, 793, 11
 Roehly, Y., Buat, V., Heinis, S., Moreau, C., & Gimenez, S. 2011, in ASP Conf. Ser. 442, *Astronomical Data Analysis Software and Systems XX*, ed. I. N. Evans et al. (San Francisco, CA: ASP), 25
 Romano, D., Matteucci, F., Zhang, Z.-Y., Papadopoulos, P. P., & Ivison, R. J. 2017, *MNRAS*, 470, 401
 Roseboom, I. G., Ivison, R. J., Greve, T. R., et al. 2012, *MNRAS*, 419, 2758
 Roseboom, I. G., Oliver, S. J., Kunz, M., et al. 2010, *MNRAS*, 409, 48
 Schuller, F. 2012, *Proc. SPIE*, 84521T
 Schuller, F., Menten, K. M., Contreras, Y., et al. 2009, *A&A*, 504, 415
 Scoville, N., Aussel, H., Sheth, K., et al. 2014, *ApJ*, 783, 84
 Scoville, N., Sheth, K., Walter, F., et al. 2015, *ApJ*, 800, 70
 Simpson, J. M., Smail, I., Swinbank, A. M., et al. 2015, *ApJ*, 799, 81
 Simpson, J. M., Swinbank, A. M., Smail, I., et al. 2014, *ApJ*, 788, 125
 Siringo, G., Kreysa, E., Kovács, A., et al. 2009, *A&A*, 497, 945
 Smolčić, V., Navarrete, F., Aravena, M., et al. 2012, arXiv:1203.5542
 Snyder, G. F., Brodwin, M., Mancone, C. M., et al. 2012, *ApJ*, 756, 114
 Spergel, D. N., Verde, L., Peiris, H. V., et al. 2003, *ApJS*, 148, 175
 Springel, V., White, S. D. M., Jenkins, A., et al. 2005, *Natur*, 435, 629
 Steidel, C. C., Giavalisco, M., Pettini, M., Dickinson, M., & Adelberger, K. L. 1996, *ApJL*, 462, L17
 Stevens, J. A., Ivison, R. J., Dunlop, J. S., et al. 2003, *Natur*, 425, 264
 Stevens, J. A., Page, M. J., Ivison, R. J., Smail, I., & Carrera, F. J. 2004, *ApJL*, 604, L17
 Strandet, M. L., Weiss, A., Vieira, J. D., et al. 2016, *ApJ*, 822, 80
 Swinbank, A. M., Simpson, J. M., Smail, I., et al. 2014, *MNRAS*, 438, 1267
 Swinbank, A. M., Smail, I., Longmore, S., et al. 2010, *Natur*, 464, 733
 Tacconi, L. J., Neri, R., Chapman, S. C., et al. 2006, *ApJ*, 640, 228
 Tamura, Y., Kohno, K., Nakanishi, K., et al. 2009, *Natur*, 459, 61
 Tanaka, M., Finoguenov, A., Mirkazemi, M., et al. 2013a, *PASJ*, 65, 17
 Tanaka, M., Toft, S., Marchesini, D., et al. 2013b, *ApJ*, 772, 113
 Thomas, D., Maraston, C., Bender, R., & Mendes de Oliveira, C. 2005, *ApJ*, 621, 673

- Thomas, D., Maraston, C., Schawinski, K., Sarzi, M., & Silk, J. 2010, [MNRAS](#), **404**, 1775
- Tozzi, P., Santos, J. S., Jee, M. J., et al. 2015, [ApJ](#), **799**, 93
- Uchiyama, H., Toshikawa, J., Kashikawa, N., et al. 2017, arXiv:1704.06050
- Valiante, E., Smith, M. W. L., Eales, S., et al. 2016, [MNRAS](#), **462**, 3146
- Vieira, J. D., Crawford, T. M., Switzer, E. R., et al. 2010, [ApJ](#), **719**, 763
- Wang, W.-H., Cowie, L. L., Barger, A. J., & Williams, J. P. 2011, [ApJL](#), **726**, L18
- Weiß, A., De Breuck, C., Marrone, D. P., et al. 2013, [ApJ](#), **767**, 88
- Weiß, A., Kovács, A., Coppin, K., et al. 2009, [ApJ](#), **707**, 1201
- White, S. D. M. 1978, [MNRAS](#), **184**, 185
- Zavala, J. A., Montaña, A., Hughes, D. H., et al. 2017, arXiv:1707.09022